Journal of
Materials Chemistry A

REVIEW

View Article Online
View Journal | View Issue

Cite this: *J. Mater. Chem. A*, 2021, **9**, 19179

Biomimetic photocatalysts for the conversion of aqueous- and gas-phase nitrogen species to molecular nitrogen *via* denitrification and ammonia oxidation

Cheolwoo Park,†[ab] Hyelim Kwak,†[a] Gun-hee Moon *[c] and Wooyul Kim *[a]

Received 30th March 2021
Accepted 30th June 2021

DOI: 10.1039/d1ta02644e

rsc.li/materials-a

Denitrification and anaerobic ammonium oxidation (anammox) are important biological processes of the nitrogen cycle that help to preserve the global ecosystem. However, indiscriminate development and global population growth result in the discharge of large amounts of nitrogen species (*e.g.*, *via* the Haber–Bosch process), particularly nitrogen oxides and ammonia, which cannot be fully digested by microorganisms and therefore accumulate in soil and water. Photocatalysts can promote the conversion of nitrogen oxides and ammonia to molecular nitrogen under the action of photogenerated electrons and holes, thus mimicking denitrifying and anammox bacteria, respectively. Herein, we review the biomimetic photocatalysts and photoelectrochemical cells used to convert aqueous and airborne nitrogen species to molecular nitrogen and shed light on the charge transfer mechanism that should be selectively controlled to favor the formation of molecular nitrogen over that of nitrogen-containing intermediates and by-products. Last but not least, we discuss the outlooks and perspectives of solar-powered molecular nitrogen recovery and suggest guidelines for the design of high-performance denitrification/anammox bacteria-like photocatalysts.

1. Introduction

Unlike ammonia (NH_3), nitrite (NO_2^-), and nitrate (NO_3^-), molecular nitrogen (N_2), which constitutes ~80% of the atmosphere by volume, is not chemically and biologically reactive and cannot therefore be utilized by plants for the synthesis of proteins to be supplied to animals and humans.[1,2] The conversion of N_2 into more reactive forms mainly occurs through microbially facilitated processes such as nitrogen fixation and

[a]Department of Chemical and Biological Engineering, Research Institute of Global Environment, Sookmyung Women's University, 99, Cheongpa-ro 47-gil, Yongsan-gu, Seoul 04310, Republic of Korea. E-mail: wkim@sookmyung.ac.kr
[b]Department of Energy Science, Sungkyunkwan University, 2066, Seobu-ro, Jangan-Gu, Suwon, Gyeonggi-do 16419, Republic of Korea
[c]Extreme Materials Research Center, Korea Institute of Science and Technology (KIST), 5. Hwarang-ro 14-gil, Seongbuk-gu, Seoul 02792, Republic of Korea. E-mail: catalysis@kist.re.kr
† These authors contributed equally.

Cheolwoo Park received a BS in Biochemical Engineering from Gangneung-Wonju National University in 2015 and is now pursuing a PhD in Energy Science under the supervision of Prof. Tae Kyu Ahn at Sungkyunkwan University (SKKU). He joined Sookmyung Women's University (advisor: Prof. Wooyul Kim) as a visiting researcher in 2016 and focuses on elucidating the reaction mechanisms of surface-modified metal oxide photocatalysts for energy conversion and environmental applications.

Hyelim Kwak received a BS in Chemical and Biological Engineering from Sookmyung Women's University (Seoul, Korea) in 2020 and is currently pursuing a master's degree under the supervision of Prof. Wooyul Kim at Sookmyung Women's University, focusing on photocatalysis for environmental and energy applications.

nitrification. The fixed reactive forms are absorbed, used, released in the form of excrements and dead bodies, converted back to the biologically inert form (*i.e.*, N_2) through denitrification and anammox, and eventually returned to the atmosphere.[1] This biological nitrogen cycle preserved the balance between nitrogen fixation and denitrification for thousands of years.[2] In the 20th century, however, human activities began to strongly impact the modern nitrogen cycle (established some 2.5 billion years ago), which is likely to result in the establishment of a new steady state in several decades.

Over the past century, the development of industrial processes and the rapid increase in fossil fuel use to satisfy the growing global demand for food and energy have drastically disrupted the nitrogen cycle.[3–9] In particular, the Haber–Bosch process offers a way to synthetically fix nitrogen in the form of ammonia for the mass production of synthetic fertilizers,[3] thus enabling abundant food production along with rapid world population growth. In the last 50 years, the consumption of fertilizers and fossil fuels has increased more than six-fold[4,5] and three-fold,[6] respectively. The projected global population growth is expected to result in elevated fertilizer production and fossil fuel consumption. As both of these anthropogenic sources (*i.e.*, the Haber–Bosch process and fossil fuel combustion) account for ∼45% of the annual fixed nitrogen production (Fig. 1a), the above increase will initiate a cascade of large-scale environmental impacts such as (i) the extensive eutrophication of terrestrial and aquatic systems, (ii) the increase in potent greenhouse gas (*i.e.*, N_2O) inventory, and (iii) global acidification. The low (typically <40%) utilization efficiency of the nitrogen contained in fertilizers results in the nitrification-based conversion of large amounts of fertilizer (∼90% of NH_4^+) to highly mobile NO_3^- ions, which can leach into aquatic systems such as rivers, lakes, and aquifers.[2] Moreover, besides producing N_2 as the main product, anaerobic denitrification also affords N_2O and thus significantly affects atmospheric N_2O levels.[7] As N_2O reacts with the stratospheric ozone and is a potent greenhouse gas with global warming potential ∼300 times that of CO_2, denitrification contributes to climate change and stratospheric ozone depletion.[7] In addition, the absorption of nitrogen compounds by agricultural soils results in their acidification and thus inhibits the activity of soil organisms and disturbs the ecosystem. Fertilizer nitrogen is easily converted into gaseous ammonia and therefore returns from the atmosphere to the watershed *via* precipitation as another reactive nitrogen form.[8] Nitrogen oxides (NO_x) produced by fossil fuel combustion not only react with ammonia to produce fine dust and ozone and thus contribute to poor air quality, but also cause acid rain and, hence, soil and ocean acidification. The nitrogen cycle, the carbon cycle, and climate are known to exhibit numerous strong mutual interactions.[9] The dramatic increase in atmospheric CO_2 levels (>30% above pre-industrial values) due to fossil fuel combustion and land use change is viewed as the primary cause of climate warming observed over the past century. The human activity-induced perturbations of global nitrogen and carbon cycles are in part related to each other, as exemplified by the possible interacting drivers of these cycles during the 21st century (Fig. 1b).

From the perspective of nitrogen cycle management, the main objectives requiring special consideration are (i) the substantial decrease in nitrogen use,[9] (ii) the direct up-cycling of

Gun-hee Moon received a BS in Chemical Engineering from Inha University (Incheon, Korea) in 2008, an MS degree in Environmental Engineering from POSTECH in 2011, and a PhD degree in Chemical Engineering from POSTECH (Pohang, Korea) in 2015. After a postdoctoral stay at the Max-Planck-Institut für Kohlenforschung (Germany, 2016–2020), he moved to the Korea Institute of Science and Technology (KIST), where he is currently employed as a senior scientist working on the design of photocatalysts, electrocatalysts, photoelectrochemical cells, and carbon materials for energy conversion and environmental applications.

Wooyul Kim received a PhD in Environmental Engineering (advisor: Prof. Wonyong Choi) from POSTECH (Pohang, Korea) in 2012 and worked at the Lawrence Berkeley National Laboratory (USA, 2012–2016) as a postdoctoral fellow (advisor: Dr Heinz Frei). During his PhD period, he joined Osaka University (advisor: Prof. Tetsuro Majima) as a visiting researcher in 2009, 2010, and 2012. He joined the faculty of the Department of Chemical and Biological Engineering at Sookmyung Women's University (Seoul, Korea) as an assistant professor (2016) and was promoted to associate professor in 2021. His current research focuses on revealing the structural identity of key intermediates and their roles in the catalytic cycle (i.e., their kinetic relevancy) to overcome the kinetic barriers for photo (or electro) catalysis. At an early stage of his independent career within the fields of photo(electro) catalysis for energy and environmental applications, he was honored as a winner of the 2020 Energy & Environmental Science lectureship award (Royal Society of Chemistry).

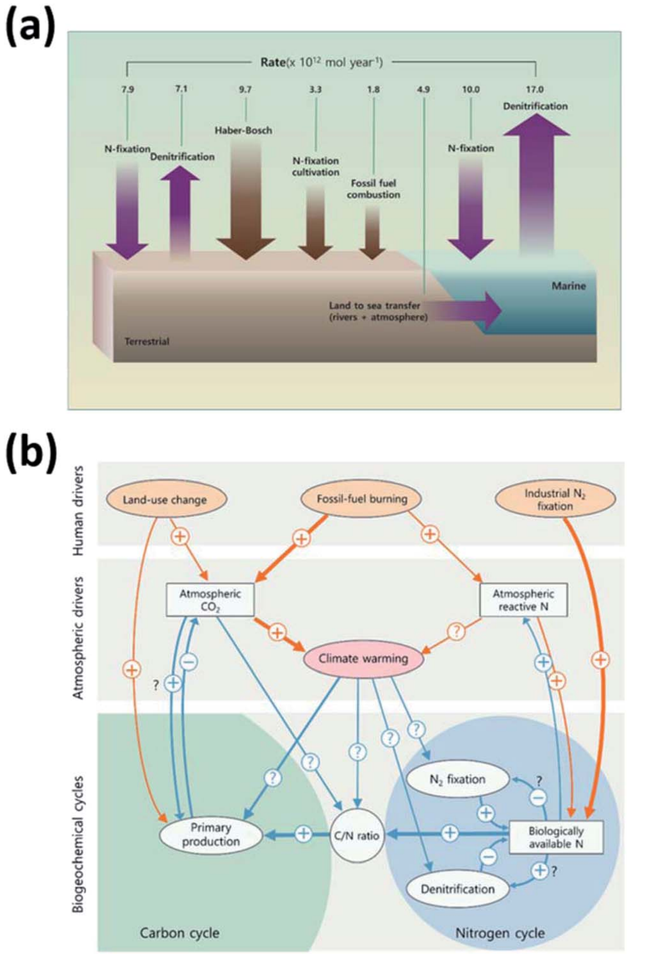

Fig. 1 (a) Rates of nitrogen flux in the modern nitrogen cycle depend on the efficiency of transformations between reservoirs. Reprinted with permission from ref. 2. Copyright© 2010, American Association for the Advancement of Science. (b) The main anthropogenic drivers of nitrogen–carbon–climate interactions in the 21st century. Reprinted with permission from ref. 9. Copyright© 2008, Nature Publishing Group.

used nitrogen to microbial protein,[10] and (iii) the development of artificial denitrification processes powered by renewable energy. Among the various methods of decreasing nitrogen use, one can mention systematic crop rotation,[10] optimization of fertilizer introduction timing and amount,[11] and the breeding/development of genetically engineered crops for increasing nitrogen use efficiency.[12] In view of the low efficiency of nitrogen utilization (*e.g.*, agricultural nitrogen utilization efficiency = 40%, feed conversion efficiency = 15%, manure utilization efficiency = 50%),[10] the direct up-cycling of used nitrogen to microbial protein has been proposed as an alternative to the formation of plant and meat proteins. As a renewable energy-powered direct denitrification process, the photocatalytic reduction of reactive nitrogen compounds to N_2 holds great promise since the advantages of photocatalysis compared with conventional catalysis, thermocatalysis, and electrocatalysis are that (i) it does not require energy-intensive processes (solar energy *vs.* heat or electricity), (ii) the operation is possible without the need for oxidants, reductants, or electrolytes, (iii) it is flexible for application in both aqueous and gas-phase reactions, and (iv) material cost is relatively cheap.[13–17] Herein, we introduce and discuss the most recent findings and advances in photocatalytic denitrification and ammonia oxidation processes, the ultimate goal of which is the conversion of reactive nitrogen compounds (*e.g.*, ionic or gas-phase nitrogen oxides, ammonia) into inert N_2 on a scale comparable to that of anthropogenic nitrogen fixation. Most parts of this review deal with denitrification/anammox bacteria-like photocatalysts and the related mechanisms, which greatly affect activity and selectivity.

2. Photocatalysts and co-catalysts for denitrification

2.1. Reduction of ionic nitrogen oxides to N_2

The nitrogen cycle imbalance due to human activities (*e.g.*, combustion, intensive fertilizer use, and agriculture) has resulted in increased nitrate levels in groundwater and other waters. Ionic nitrogen oxides including nitrate, nitrite, and NO^- are the prevalent contaminants in groundwater, causing eutrophication, water waste, and potentially health-threatening consequences such as cancer, birth defects, and cyanosis. Therefore, the release of ionic nitrogen oxides is strictly regulated, and their removal to secure water resources is a great challenge. Traditionally, the removal of NO_3^- from wastewater is achieved using reverse osmosis, ion exchange, and biological/catalytic treatment.[1,18,19]

Among the various denitrification methods used to reduce ionic nitrogen oxides in aquatic environments, eco-friendly photocatalytic denitrification is the one most promising from the perspective of industrialization.[20–22] This photocatalytic reduction affords inert N_2 gas and mainly involves the reduction of NO_3^- to N_2 *via* NO_2^-.[20,23–27] To increase the overall efficiency and selectivity for N_2 formation, one needs to fully understand the underlying mechanisms, including those of the undesired nitrification (conversion of NO_2^- to NO_3^-)[28,29] and the dissimilatory nitrate reduction to ammonium (DNRA).[30,31] In particular, these undesired reactions need to be precisely controlled (*i.e.*, inhibited) to maximize N_2 formation selectivity. However, from the perspective of reactive nitrogen up-cycling, the highly selective production of ammonium (*e.g.*, DNRA) could be useful.[32,33] In this section, we critically investigate the efforts made to enhance the selectivity for N_2 production in the photocatalytic denitrification of ionic nitrogen oxides and the efficiency of this process. In particular, we demonstrate the important roles of intrinsic photocatalyst properties, sacrificial agents, and specific reaction conditions.

2.1.1. Photocatalytic materials for ionic nitrogen oxide reduction to N_2. The discovery of the photocatalytic reduction of NO_3^- to NH_4^+ in aqueous solutions (over Pt–TiO$_2$) in 1987 [34] triggered the search for other denitrification photocatalysts. In nature, the corresponding reaction involves multiple-electron transfer and is primarily performed by bacteria such as *Thiobacillus denitrificans* ($2NO_3^- + 10e^- + 12H^+ \rightarrow N_2 + 6H_2O$), whereas photocatalytic denitrification predominantly occurs in a stepwise manner and involves the reduction of NO_3^- to NO_2^- and the subsequent reduction of NO_2^- to N_2 or NH_4^+.[20,35–38] Each step of the nitrate-to-N_2 reduction has its own rate constant, which is largely determined by the interaction between the photocatalyst and the adsorbed reactants (*e.g.*, NO_3^-, NO_2^-, NO, and N_2O) and reflects the ease of reactant adsorption on or product desorption from the photocatalyst.[39] Attempts to accelerate photocatalytic denitrification have resulted in the discovery and evaluation of numerous photocatalysts, among which TiO_2 is the one most frequently and thoroughly studied because of its durability, non-toxicity, long diffusion length of charge carriers, and other advantages. In particular, various methods of photocatalyst surface modification have been developed to accelerate photoconversion or alter the reaction mechanism and thus control selectivity. According to surface modifier type, these methods are classified into those relying on metal deposition,[40,41] inorganic adsorbates,[42,43] polymer coatings, dye sensitization,[44–47] impurity doping, charge transfer complexation,[48,49] *etc.* Photocatalyst modification not only increases photoconversion efficiency but also affects selectivity by influencing the mechanism and kinetics of photocatalytic denitrification. Recent studies on photocatalysis by surface-modified semiconductors are summarized below.

Photocatalysts based on pristine TiO_2 and related (bi)metallic composites. Compared to TiO_2 powder (P25), TiO_2 nanotubes (TNTs) achieved a $\sim$50% higher NO_3^- conversion efficiency and a slightly elevated selectivity for N_2 formation, which was ascribed to their high specific surface area and abundant active sites.[21] Given that bare TiO_2 exhibits poor selectivity for N_2 formation, TiO_2–metal composites (M/TiO_2) have been used for NO_3^- reduction in aquatic environments. The deposited metal changes the reactant adsorption properties and the charge carrier dynamics under illumination by modifying surface properties such as the space-charge region and charge density. In particular, metals deposited on TiO_2 promote its use as an electron sink (with the formation of a Schottky barrier potential) by decreasing the work function and, hence, increasing the electron affinity.[20] Sá *et al.* reported that the deposition of Cu, Fe, and Ag on TiO_2 increased its activity and selectivity for N_2, suggesting that the conversion efficiency and selectivity strongly depend on factors such as reaction temperature, hole scavenger presence/type, metal deposition method, and TiO_2 particle size. Among the various M/TiO_2 composites, Ag/TiO_2 showed the highest activity to meet the EU-stipulated levels for drinking water (Table 1).[50] The surface plasmon resonance effect of Ag^0 and Au^0 on TiO_2 extended the excitation range of this oxide semiconductor from UV to visible and promoted the separation of photogenerated charge carriers (Fig. 2a).[51] Compared to other M/TiO_2 composites, Ag/TiO_2 exhibited high selectivity for the reduction of NO_3^- to N_2,[21,40,41] while Au/TiO_2 accelerated the formation of NH_4^+.[51] The non-noble metals/TiO_2 (Cu, Ni, Fe, Bi, Zn, *etc.*) composites also exhibited enhanced catalytic performance.[33,52–54] For instance, Fe/TiO_2 and Zn/TiO_2 exhibited better N_2 yield and selectivity than bare TiO_2.[54–56] Regarding Cu/TiO_2 and Ni/TiO_2, the formation of NO_2^- and NH_4^+ was predominant, where the nitrate reduction was facilitated by the electrons accumulated on Cu or Ni but the interaction with intermediates inhibited the generation of N_2.[33,50,54] On the other hand, Cr/TiO_2 and Co/TiO_2 lowered the conversion of NO_3^-, which was explained by the light shield effect at a specific wavelength and the fast charge recombination kinetics as well.[33,54] However, conventional metal-modified photocatalysts usually suffer from metal leaching, aggregation, and gradual deactivation and need to be substantially optimized in terms of N_2 formation selectivity.

In bimetallic composites, the metals act as promoters and selectors. The promoter metal (*e.g.*, Cu, Sn, In)[57–59] initiates the rate-limiting step of the NO_3^- to NO_2^- conversion, while the selector metal (*e.g.*, Pd, Pt, Rh)[60,61] further reduces NO_2^- to NH_4^+ and/or N_2. Among the available metal combinations, Pd–Cu is widely accepted as the most active and selective one for electrocatalytic NO_3^- reduction, the mechanism of which has been revealed by conventional electrochemical analysis and density functional theory (DFT) calculations.[45,46] The increased H_2 amount resulting from the elevated Pd loading and H_2 flow rate promoted the reduction of Cu^{II} to Cu^0 and thus facilitated NO_3^- removal, while the high N : H ratio on the active Pd sites increased the selectivity for N_2.[62] Bimetallic electrocatalysts have been widely deposited on photocatalysts for photocatalytic applications.[63] Precious metal (*e.g.*, Pt, Pd)–Cu combinations are among those offering the highest activity and selectivity for catalytic NO_3^- reduction (Table 1). Notably, NO_3^- was mainly converted to ammonia (over Pt/TiO_2) or NO_2^- (over Cu/TiO_2), whereas Pt–Cu/TiO_2 catalysts exhibited a considerable selectivity for N_2 formation in photocatalytic NO_3^- reduction.[64] The fact that N_2 formation was observed for Pd/TiO_2 and Pd–Cu/TiO_2 systems but was negligible for the Cu–TiO_2 system means that Pd is indispensable for the photocatalytic reduction of NO_2^- to N_2.[65,66] Likewise, in bimetallic composites, electrons transferred from TiO_2 to promoter metal sites reduce NO_3^- to NO_2^-, with the subsequent reduction of NO_2^- to N_2 occurring at selector metal sites. The adsorption of protons on the selector metal surface significantly affects the overall selectivity for N_2 (Fig. 2b). Hence, the metal deposited on TiO_2 controls the reaction path and, hence, the conversion efficiency and selectivity for N_2 or NH_4^+, which implies that the optimization of the promoter-to-selector metal ratio is crucial for realizing selective N_2 formation. Finally, the presence of sacrificial electron donors and the occurrence of competitive reactions (*e.g.*, H_2 production) present additional challenges.

New photocatalyst types. Much effort has been directed at the optimization of perovskite-based photocatalysts, as the unique properties of perovskites (*e.g.*, chemical and optical stability, tunable bandgap and crystal structure, and long charge carrier lifetime) allow one to readily alter the dynamics of photogenerated charge carriers and the overall photocatalysis mechanism. $Pd/GdCrO_3$ exhibited faster nitrate reduction and higher selectivity for N_2 due to the negative conduction band energy level and the co-catalyst effect of Pd,[67] while $FeTiO_3$ was characterized by negligible NH_4^+ formation (*i.e.*, it exhibited a remarkably high selectivity for N_2) without the need for complex and expensive catalysts.[68] $KTaO_3$ effectively promoted the photocatalytic reduction of NO_3^- to NO_2^-, N_2, and NH_3

Table 1 Materials used for the photocatalytic reduction of ionic nitrogen oxides

No.	Photocatalyst	Co-catalyst	Light	Initial conc.	Catalyst loading ($g\ L^{-1}$)	Sacrificial reagent	NO_3^- conversion (%)	N_2 selectivity (%)	By-products	Ref.
1	TiO_2	—	Medium-pressure Hg lamp, 150 W	1 mM	2.5	Oxalic acid	15	—	NH_4^+	82
2	TiO_2	—	Medium-pressure Hg lamp, 400 W	10 mM	10	Oxalic acid	9.8	56.5	NO_2^-, NH_4^+	33
3	TiO_2	—	Medium-pressure Hg lamp, 150 W	0.8 mM	0.45	Oxalic acid	90.1	55.4	NO_2^-, NH_4^+	68
4	TiO_2	—	High-pressure Hg lamp, 100 W	0.8 mM	0.38	Formic acid	48.5	38.1	NO_2^-, NH_4^+	80
5						KI	25.5	18		
6	TiO_2	—	High-pressure Hg lamp, 300 W	1.6 mM	1	Formic acid	26.8	72.4	NO_2^-, NH_4^+	81
7	TiO_2	—	High-pressure Hg lamp, 150 W	1.6 mM	1	Formic acid	35.8	87.7	NO_2^-, NH_4^+	21
8	TiO_2 (TNTs)						53.3	89.5	NO_2^-, NH_4^+	
9	TiO_2	Au	400 W lamp	1.6 mM	0.21	Oxalic acid	44	—	NH_4^+	83
10	TiO_2	Cu	High-pressure Hg lamp, 110 W	100 ppm	0.38	Formic acid	100	63	NH_4^+	50
11	TiO_2	Ag	High-pressure Hg lamp, 300 W	1.6 mM	1	Formic acid	99.6	88.4	NO_2^-, NH_4^+	81
12	TiO_2	Ag_2O					97.5	82.9	NO_2^-, NH_4^+	
13	TiO_2 (TNTs)	AgCl	High-pressure Hg lamp, 150 W	1.6 mM	1	Formic acid	94.5	92.9	NO_2^-, NH_4^+	21
14	TiO_2	Pt–Cu	High-pressure Hg lamp, 250 W	60 $mg\ L^{-1}$	1	Benzene	59	∼89	NO_2^-, NH_4^+	64
15	TiO_2	Pd–Cu	High-pressure Hg lamp, 400 W	0.05 mM	100	Formic acid	56	98	NO_2^-	65
16	TiO_2	Pd–Cu	Medium-pressure Hg lamp, 150 W	1.6 mM	0.52	Formic acid 0.08 M	84	83	NO_2^-, NH_4^+	66
17	$LiNbO_3$	—	High-pressure Hg lamp, 100 W	0.8 mM	0.38	Formic acid	98.4	95.8	NO_2^-, NH_4^+	80
18		—	High-pressure Hg lamp, 100 W	0.8 mM	0.38	KI	96.2	93	NO_2^-, NH_4^+	
19	$LiNbO_3$	—	UV lamp	10 $mg\ L^{-1}$	Membrane	Formic acid	81.82	98.04	NO_2^-, NH_4^+	22
20	$LiNbO_3$	—	High-pressure Hg lamp, 100 W	0.8 mM	0.4	Formic acid	60.5	57.21	NO_2^-, NH_4^+	76
21		Fe					86.69	85.71	NO_2^-, NH_4^+	
22	$CuInS_2$	0.75 wt%	Hg lamp, 125 W	7.2 $mg\ L^{-1}$	0.5	Sodium oxalate	100	80.2	NO_2^-	77
23		Pt–0.75 wt% Ru	Xe lamp, 300 W (400 nm cut-off)				100	56.1	NO_2^-	
24	$FeTiO_3$		Medium-pressure Hg lamp, 150 W	0.8 mM	0.45	Oxalic acid	100	93	NO_2^-	68
25	$GdCrO_3$	1 wt% Pd	High-pressure Hg lamp, 500 W	0.8 mM	0.5	Formic acid 0.4 mM	98.7	100	—	67
26		1 wt% Ag					85.1	83.2	NO_2^-, NH_4^+	
27		1 wt% Cu					81.9	78.8	NO_2^-, NH_4^+	
28		—					79.3	81.4	NO_2^-, NH_4^+	
29	$CuFe_{0.7}Cr_{0.3}S_2$	0.75 wt% Pd 3 wt% Au	Hg lamp, 500 W	1.6 mM	1	Sodium oxalate	100	59	NO_2^-	78
30	$KTaO_3$	1 wt% Ni	High-pressure Hg lamp, 450 W	10 mM	2.5	—	97	44	H_2, NO_2^-, NH_4^+	69

under UV light irradiation even in the absence of co-catalysts or reducing reagents such as organic compounds.[69]

Layered double hydroxides (LDHs) with hydrotalcite-like structures are some of the interesting materials due to their unique properties such as anions intercalated in 2D interlayer spaces, a bunch of surface hydroxyl groups, flexibility to change elements, and swelling nature, where divalent (*e.g.*, Mg, Co, Ni, Cu, and Zn) and trivalent (*e.g.*, Al, Cr, Ni, and Ga) metal cations are combined.[70,71] In particular, a high specific surface area, excellent electrical conductivity, high mobility of charge carriers, and high chemical stability make it possible to apply them in various photocatalytic reactions.[72–74] Therefore, it was reported that the MgAl-LDH used for NO_3^- reduction enhanced the selectivity to N_2 without any sacrificial reagent, which was ascribed to both attraction of NO_3^- ions near the photocatalyst surface and restriction of charge carrier recombination.[75]

$LiNbO_3$ is a nonlinear optical material with high potential for NO_3^- removal,[22,60,76] offering spontaneous polarization screening by either free electrons and holes or ions/molecules adsorbed on the surface. The second harmonic generation effects of nonlinear optical materials facilitate the generation of electrons and inhibit the recombination of charge carriers to

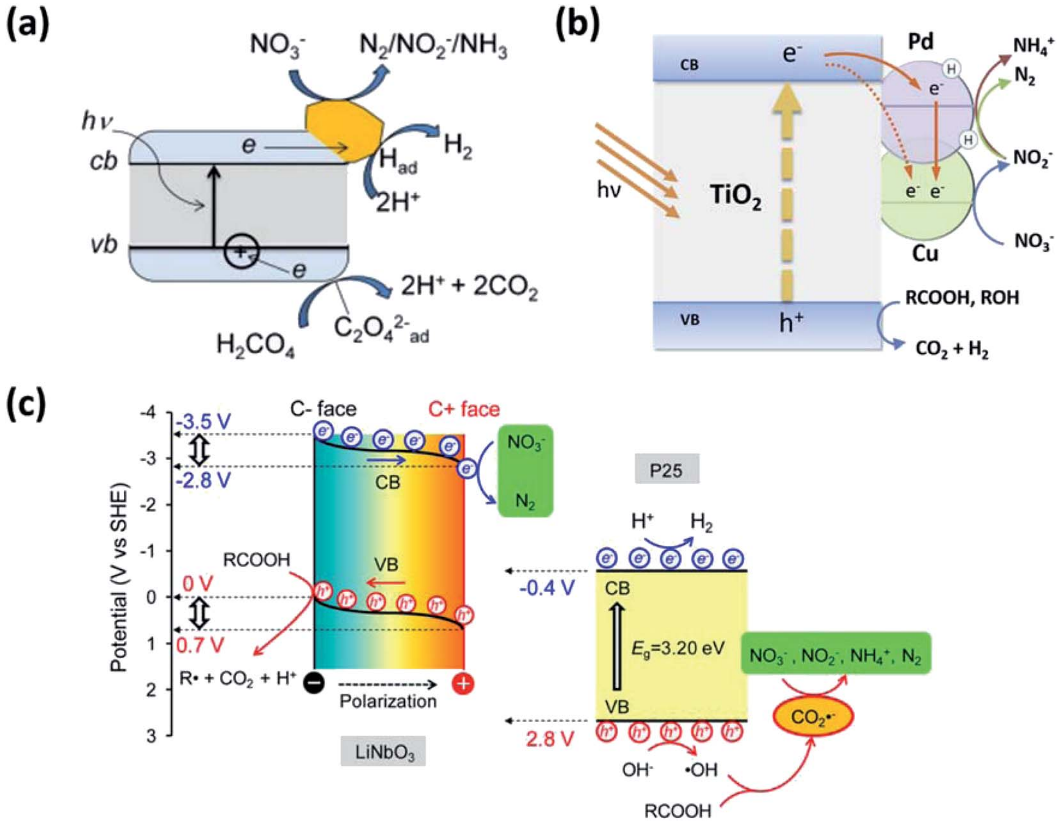

Fig. 2 Photocatalytic nitrate reduction promoted by (a) Au/TiO_2 and (b) Pd–Cu/TiO_2. Reprinted with permission from ref. 51 and 66. Copyright© 2011 and 2014, Elsevier. (c) Comparison of nitrate reduction promoted by $LiNbO_3$ and P25 TiO_2. Reprinted with permission from ref. 80. Copyright© 2016, American Chemical Society.

enhance the efficiency and stability of NO_3^- reduction. The superior (compared to that of bare TiO_2) activity of $LiNbO_3$ was attributed to the photocatalytic reduction of nitrate through direct heterogeneous interactions with electrons at the conduction band of this material, whereas in the conventional photocatalysis mechanism, nitrate is mainly reduced by $CO_2^{\bullet-}$ generated from holes at the valence band (Fig. 2c). In an effort to develop a systematic and durable industrial-scale process, $LiNbO_3$ was applied to a membrane platform,[22] which offered the inherent benefits of high separation performance and antifouling properties compared to common ultrafiltration membranes. In addition, $LiNbO_3$ has been successfully applied to membrane materials without significant photocatalytic activity inhibition (Table 1). Fe–$LiNbO_3$ exhibited an enhanced selectivity for N_2 formation as well as a high NO_3^- conversion efficiency,[76] which was ascribed to the increase in the specific surface area and the number of Lewis-acidic sites upon doping.

As wide-bandgap semiconductors (*e.g.*, TiO_2, $FeTiO_3$, $GdCrO_3$, and $KTaO_3$) are intrinsic UV-light-driven photocatalysts, a more effective strategy would be to develop narrow-bandgap photocatalysts and thus utilize the whole solar spectrum. As a result, various chalcogenide materials (*e.g.*, $CuInS_2$ [77] and $CuFe_{0.7}Cr_{0.3}S_2$ [78]) have been developed. In particular, $CuInS_2$ has a narrow bandgap of 1.45 eV and an insufficient conduction band potential for H_2 production, thus preventing the over-reduction of nitrate to ammonia.

2.1.2. Insights into the mechanism of ionic nitrogen oxide reduction. The efficiency and selectivity of artificial solar denitrification systems can be increased by suppressing undesired reactions, which mainly correspond to DNRA (*i.e.*, ammonification) and the re-oxidation of NO_2^- to NO_3^-. In turn, a deep understanding of the overall mechanism is required to precisely control competitive reactions and thus selectively convert ionic nitrogen species to N_2 while maintaining sufficient catalytic rates for keeping up with the photon flux at maximum solar intensity. DNRA is widely known as the anaerobic microbial pathway of the natural nitrogen cycle. The important implication of DNRA in denitrification is the production of NH_4^+ from NO_3^-, which is the major side reaction for the reduction of NO_3^- to N_2. The NO_2^- ion produced by the reduction of NO_3^- ($NO_3^- + 2e^- + 2H^+ \rightarrow NO_2^- + H_2O$) can undergo ammonification ($NO_2^- + 6e^- + 8H^+ \rightarrow NH_4^+ + 2H_2O$) or denitrification ($NO_2^- + 6e^- + 8H^+ \rightarrow N_2 + 4H_2O$), both of which are six-electron reductions. The preference for a particular NO_2^- reduction pathway is strongly affected by the environment, particularly by the ratio of N species to H atoms (N : H ratio) at active sites. The injection of excess H_2 increases the surface concentration of H^+ at active sites because of the low-energy-barrier dissociative adsorption of H_2 and thus increases the selectivity for NH_4^+ formation (Fig. 3a). Alternatively, the N : H ratio can be changed by controlling the steady-state concentration of NO_2^- to increase the probability of binding of two nitrogen species to

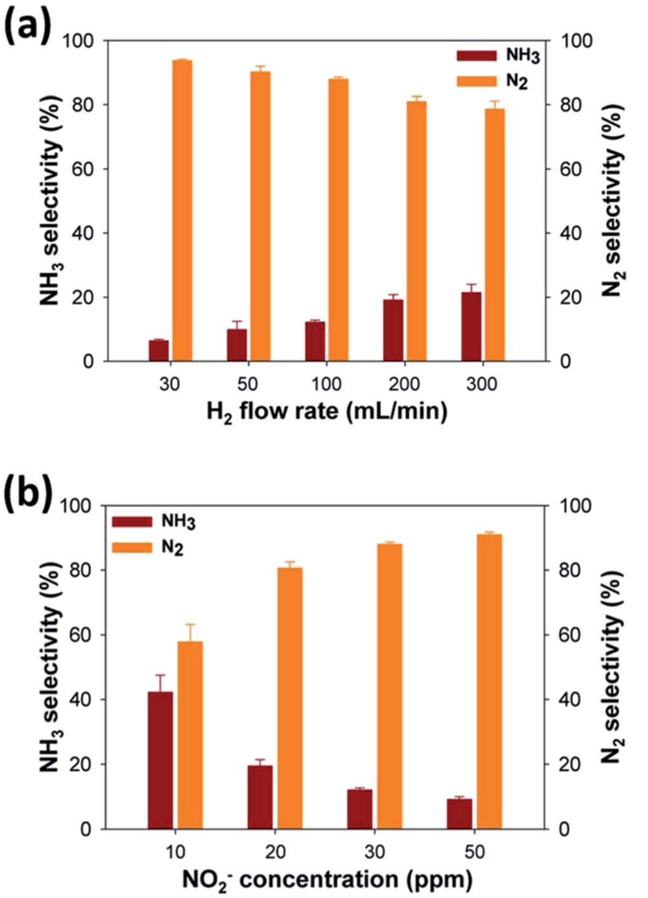

Fig. 3 Dependence of product (N_2 and NH_3) selectivity during NO_2^- reduction over Pd/TiO_2 on (a) H_2 flow rate and (b) NO_2^- concentration. Reprinted with permission from ref. 60. Copyright© 2014, American Chemical Society.

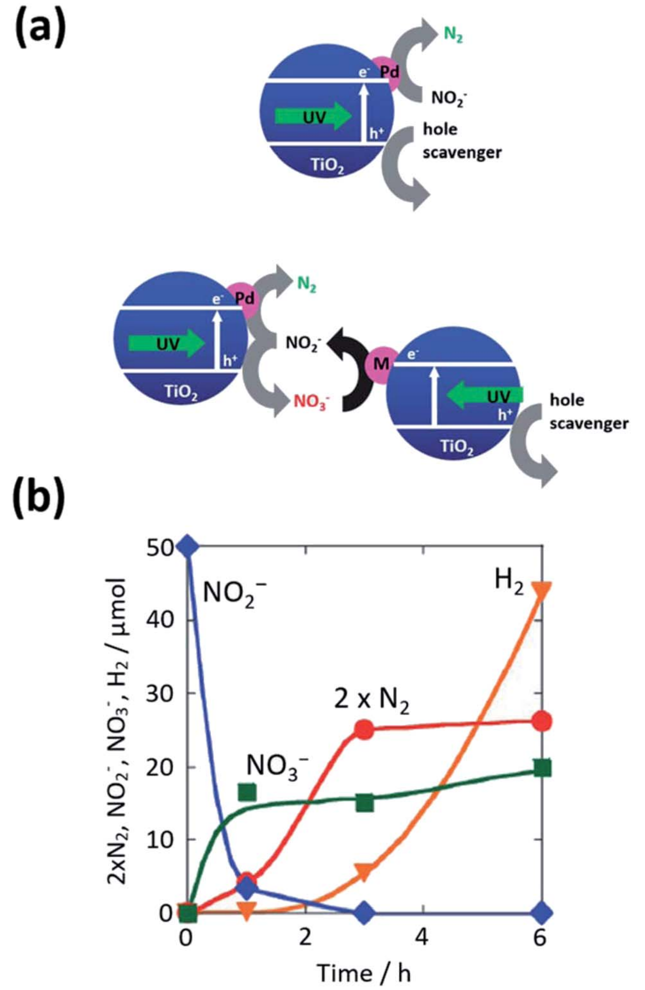

Fig. 4 (a) Schematic mechanism of Pd/TiO_2 operation and the combination of two photocatalytic systems for the reduction of NO_2^- to N_2 and NO_3^-. (b) Time-dependent conversion of NO_2^- and the formation of N_2, H_2, and NO_3^- in suspensions of Pd–TiO_2 in aqueous sodium oxalate (diamonds: NO_2^-, circles: N_2, squares: NO_3^-, triangles: H_2). Reprinted with permission from ref. 29. Copyright© 2012, Royal Society of Chemistry.

form N_2 (Fig. 3b). The fine-tuning of the N : H ratio at surface active sites is required to suppress DNRA and thus selectively convert NO_2^- to N_2.

In the case of efficient nitrate conversion, photocatalytic nitrite oxidation, which is hard to detect during NO_3^- reduction, should be considered for low-efficiency nitrate reduction. Even if nitrification and denitrification occur simultaneously, it is difficult to identify the main factors of nitrification because of the same initial reactant and product. The formation of NO_3^- indicates that the oxidation of NO_2^- by holes occurs even in the presence of a hole scavenger in aqueous photocatalyst suspensions (Fig. 4). The low NO_3^- conversion efficiency is due to the low rate constant of NO_3^- reduction and the high rate constant of NO_2^- oxidation.

The minimal loss of photogenerated electron–hole pairs offers flexibility for maximizing photocatalytic efficiency by adding sacrificial hole or electron scavengers to restrict charge carrier recombination. Sacrificial electron donors (*i.e.*, hole scavengers) were used for photocatalytic denitrification in aqueous media to enable the efficient reduction of ionic nitrogen species[5] and were shown to affect reactant–photocatalyst interactions. Sacrificial reagents act not only as efficient hole scavengers but also as precursors of active radicals for ionic nitrogen oxide reduction. Sacrificial reagents were demonstrated to promote the efficient removal of holes and thus reduce charge carrier recombination while being oxidized[34] to afford strongly reducing (−1.81 *vs.* SHE) carboxyl radicals ($CO_2^{\bullet-}$), which also resulted in activity enhancement.[79] The most common sacrificial reagents are organic compounds such as formic acid,[21,80,81] oxalic acid,[68,82,83] humic acid,[84] and methanol.[34] Among them, formic acid is the best hole scavenger for NO_3^- reduction, as its simple structure results in the exclusive formation of the strongly reducing $CO_2^{\bullet-}$, while the release of protons promotes efficient N_2-selective reduction. Oxalic acid is the second most used hole scavenger, featuring a higher selectivity for NH_4^+ formation than formic acid (Table 1). The dependence of selectivity on hole scavenger type is attributed to the reduction ability of the reactant and intermediates. Simple carboxyl compounds (formic acid, sodium

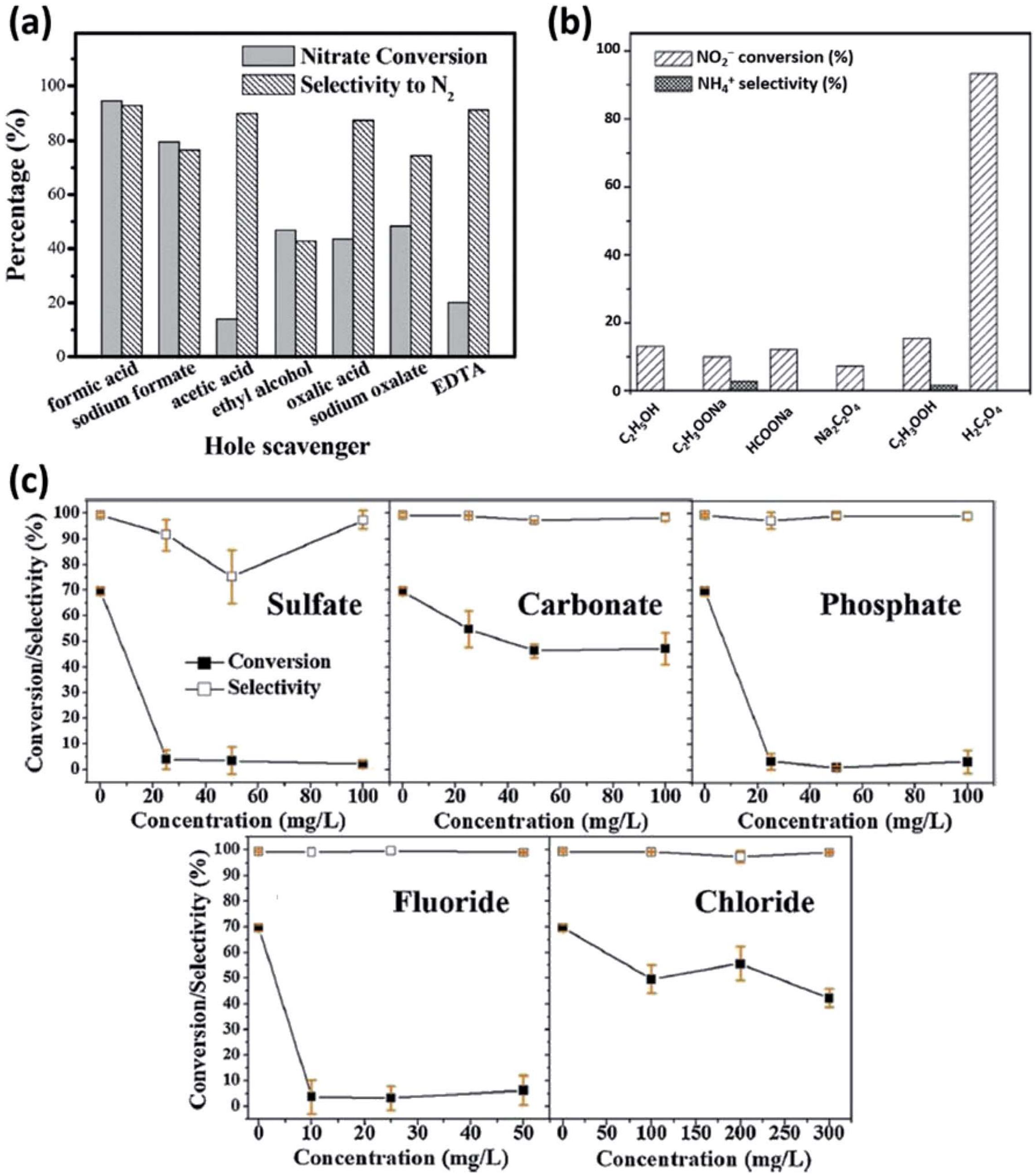

Fig. 5 (a) Effects of organic hole scavengers on the reduction of NO_3^- over $AgCl/TiO_2$ nanotubes. Reprinted with permission from ref. 21. Copyright© 2018, Royal Society of Chemistry. (b) Effects of organic hole scavengers on the reduction of NO_2^- over Ag/TiO_2. Reprinted with permission from ref. 85. Copyright© 2007, American Chemical Society. (c) Photocatalytic nitrate conversion efficiency and N_2 selectivity achieved over TiO_2 in the presence of different levels of SO_4^{2-}, HCO_3^-, $H_2PO_4^-$, F^- and Cl^- (irradiation duration: 3 h, sacrificial agent: formic acid). Reprinted with permission from ref. 86. Copyright© 2020, Elsevier.

formate, *etc.*) are oxidized to afford abundant $CO_2^{\bullet -}$ radicals and therefore allow for more efficient conversion than other organic hole scavengers. On the other hand, oxalic acid remarkably enhances the conversion of nitrite to N_2 while exhibiting a modest hole scavenging ability (Fig. 5a and b).[21,85] The understanding of the complicated interactions between various intermediates and sacrificial reagents is particularly challenging in the case of photocatalytic denitrification. In addition, the presence of additional reagents such as SO_4^{2-}, $H_2PO_4^-$, F^-, Cl^-, and HCO_3^- increases system complexity and therefore leads to hole blocking and, as a consequence, inhibits hole scavenger oxidation by promoting surface anionization (Fig. 5c).[86]

2.2. Denitrification of airborne NO_x and N_2O to N_2

Airborne nitrogen oxides (NO_x) including NO and NO_2 originate from anthropogenic (combustion of fossil fuels at high temperatures in automobile engines and power plants) and biogenic sources, significantly affecting human health and the environment.[87] N_2O is produced by human activities and natural processes and is both a greenhouse gas and an ozone-depleting substance.[88] Taken together, NO_x and N_2O significantly affect the environment *via* (i) ozone and smog generation due to the reaction of NO_x with volatile organic compounds (VOCs) upon irradiation with light, (ii) the acidification of water vapor (acid rain), (iii) excessive algal growth due to the dissolution of NO_x in water (eutrophication), (iv) climate change and ozone layer depletion, and (v) secondary fine dust formation through the combination of the above oxides with water vapor, O_3, ammonia, *etc.* Selective catalytic reduction (SCR)-based denitrification is a long-standing industrial process that is used to control air quality and is performed using different types of reactors and catalysts, depending on the application. Regarding the conventional deNO_x process, ammonia has been used as a reducing agent instead of hydrogen to improve process safety and reduce the operating temperature.[89] The conversion of NO_x to N_2 is described by Eley–Rideal and Langmuir–Hinshelwood models, which rely on the decomposition of intermediates generated through the reaction of surface-adsorbed activated NH_3 with free gaseous NO and NO adsorbed on basic catalyst sites, respectively. Alternatively, airborne NO_x can be removed *via* complete oxidation to NO_3^-. Although this approach (nitrification) has received widespread attention for the development of smart cement and asphalt used in the construction of the state-of-the-art urban infrastructure,[90] the accumulation of NO_3^- on the surface of photocatalysts can result in their deactivation. As this review focuses on denitrification only, readers interested in solar-driven nitrification are advised to consult appropriate literature.

The photocatalytic reduction of NO_x and N_2O to N_2 offers the following advantages: (i) the use of water instead of the explosive H_2 and the toxic NH_3, (ii) operation at standard temperature and pressure, (iii) net zero carbon emission for operation under natural sunlight, and (iv) the availability of cheap and environmentally benign materials.[91–94] As electron–hole pairs photogenerated in semiconducting materials can be transformed to the strongly oxidizing reactive oxygen species (ROS), aerobic conditions favor nitrification, in which case O_2 acts as a good electron acceptor and a precursor of mobile hydroxyl radicals ($O_2 + H^+ + e^- \rightarrow HO_2^{\bullet}$, $HO_2^{\bullet} + H^+ + e^- \rightarrow H_2O_2$, $H_2O_2 + e^- \rightarrow OH^- + OH^{\bullet}$).[95] Under anaerobic conditions, the electrons can be transferred to NO_x or N_2O without interference from O_2 but can still be intercepted by water vapor ($2H_2O + 2e^- \rightarrow H_2 + 2OH^-$) (Fig. 6). Ideally, the residual holes in photocatalysts oxidize water vapor ($2H_2O + 4h^+ \rightarrow O_2 + 4H^+$), otherwise, nitrification is driven by oxidation with holes or $OH^{\bullet}$ ($H_2O + h^+ \rightarrow OH^{\bullet} + H^+$). Along with selective charge transfer, other problems such as low solar light absorption, poor catalytic activity, need for noble metal–based co-catalysts, and lack of long-term durability should be overcome for practical applications. Herein, we summarize the strategies (*e.g.*, structure and morphology control, co-catalyst loading, heteroatom doping, and hybridization with different types of materials) used to address the weaknesses of the photocatalytic reduction of NO_x and N_2O to N_2.

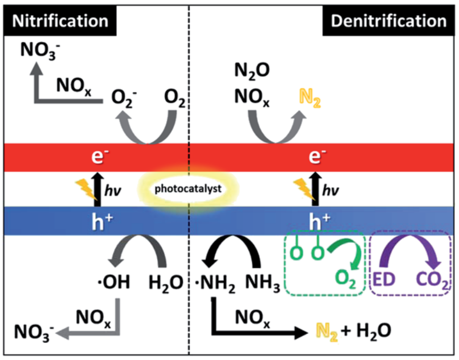

Fig. 6 Comparison of photocatalytic nitrification (left panel) and denitrification (right panel) mechanisms. The bottom right panel presents NH_3-mediated denitrification, the release of trapped oxygen atoms from NO (green box), and the oxidation of sacrificial gases (purple box; ED stands for carbon-containing electron donors such as CO, CH_4, C_3H_8, CH_3OH, and C_2H_5OH).

2.2.1. Photocatalysts for the reduction of airborne NO_x to N_2

DeNO$_x$ without additional electron donors. Water vapor and surface-trapped oxygen atoms formed by electron transfer to NO are ideal electron donors for the photocatalytic denitrification of NO_x; however, the kinetics of water oxidation is sluggish, and the control of selective electron transfer to NO_x is difficult. Therefore, whereas most studies focus on photocatalyst structure/surface modification and the operation of deNO_x in the presence of nitrogen- or carbon-containing electron donors (*e.g.*, NH_3, CO, CH_4, C_3H_8, CH_3OH, and C_2H_5OH), very few processes have been performed without these donors. Wu *et al.* optimized the selectivity of NO reduction to N_2 by controlling oxygen vacancies in TiO_2 nanoparticles.[96] These vacancies were introduced by doping the TiO_2 lattice with Fe^{3+}, and the substitution of Ti^{4+} by Fe^{3+} contributed to the charge compensation between negatively charged dopants and positively charged oxygen vacancies.[97] In air, the photocatalytic conversion of NO over pristine TiO_2 was not selective for N_2 (Fig. 7a and Table 2), whereas a significantly improved selectivity was observed for Fe-doped TiO_2 (Fig. 7b). The highest yield and selectivity for N_2 were obtained under anaerobic conditions, and the formation of NO_2 over Fe-doped TiO_2 was completely suppressed (Fig. 7c). Thus, only N_2 and O_2 were detected along with unreacted NO in the outlet (Fig. 7d). The proposed mechanism (Table 3) is believed to involve ROS (superoxide anion radicals and hydroxyl radicals) as nitrification agents. On the other hand, oxygen vacancies stabilized by Fe doping enhanced selective charge transfer to NO, which did not involve radical species, providing a clue to the design of highly effective denitrification photocatalysts.

Likewise, according to Dong *et al.*,[98] the carbon vacancy tailoring of graphitic carbon nitride (g-C_3N_4) nanosheets (C_v-g-C_3N_4) significantly enhanced NO reduction under visible light irradiation (Fig. 8a). This reduction was faster in air than in

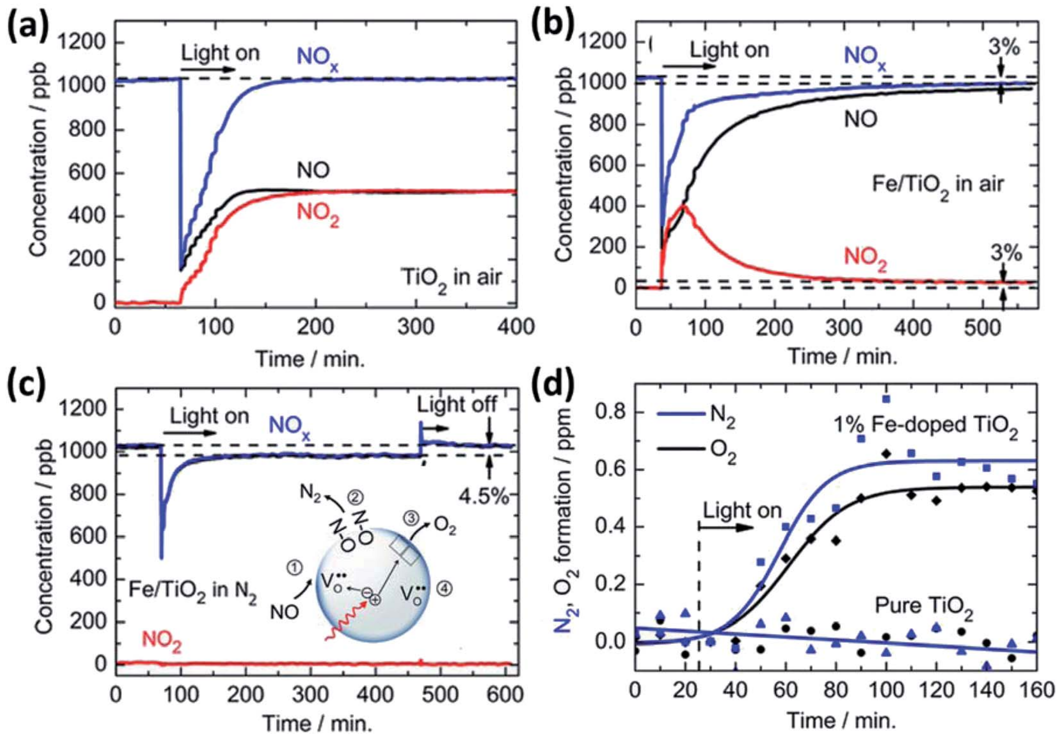

Fig. 7 Photocatalytic conversion of NO under UV light irradiation in air over (a) pristine TiO_2 and (b) Fe-doped TiO_2. (c) Photocatalytic conversion of NO to N_2 over Fe-doped TiO_2 and the schematic mechanism of this conversion. The rapid decrease of NO in (a–c) is due to the formation of NO_3^- *via* a reaction with superoxide anion radicals produced from adsorbed oxygen. (d) NO conversion ([NO] = 100 ppm) to N_2 and O_2 over pristine TiO_2 and Fe-doped TiO_2 in He. Reprinted with permission from ref. 96. Copyright© 2012, American Chemical Society.

argon irrespective of structure modification, as the ROS-mediated oxidation of NO to NO_2 is much more favorable under oxic conditions (Fig. 8b). While the photocatalytic removal of NO over g-C_3N_4 was almost prohibited under anaerobic conditions, C_v-g-C_3N_4 was characterized by a relatively high conversion of NO and high selectivity for N_2 formation (Fig. 8c), as in the case of Fe-doped TiO_2. In line with the enhanced light absorption of C_v-g-C_3N_4 and the restricted recombination of charge carriers therein, electron spin resonance (ESR) spectra suggested that surface adsorption sites stimulated the chemisorption of airborne NO (*via* the interaction between a carbon atom with an unpaired electron in g-C_3N_4 and a nitrogen atom with an unpaired electron in NO), with carbon vacancies acting as active centers to induce interactions with the NO oxygen (*i.e.*, C_v–O–N). Thus, after the adsorption of NO on g-C_3N_4 and C_v-g-C_3N_4, the ESR signal intensity due to carbon atoms with unpaired electrons decreased and increased, respectively (Fig. 8d and e). Illumination of C_v-g-C_3N_4 with pre-adsorbed NO induced a peak shift and the appearance of two new peaks at 3535 and 3555 G, which indicated the change of defect sites and the decomposition of NO into atomic N and O, respectively (Fig. 8f).

Prior to the strategies described above, Anpo *et al.* reported the UV light-promoted decomposition of NO into N_2 and O_2 over cation-exchanged ZSM-5 (Cu^+, Ag^+, and Pb^{2+}),[99–101] vanadium silicate (VS)/ZSM-5,[102] and Ti-MCM-41.[103] Herein, we do not discuss the characteristics of such materials and the corresponding kinetic analysis in detail because of the multitude of related reviews[104–106] but briefly overview the concept of transition metal ion-mediated electron transfer to NO. Cu^+ and Ag^+ immobilized in zeolites can be excited under illumination and transfer an electron to the π-antibonding orbital of NO while concomitantly accepting the electron of another NO molecule. Consequently, two contiguous N···O species adsorbed at metal ion sites are converted into N_2 and O_2. Moreover, the coordination and distribution of metal oxide species, *e.g.*, four-fold tetrahedrally coordinated vanadium oxide species with a terminal oxovanadium group (V=O) in VS/ASM-5 and Ti oxide species with tetrahedrally coordinated Ti^{4+} in Ti-MCM-41, strongly affected NO removal activity and selectivity. Although several studies demonstrated the selective conversion of NO to N_2 in the absence of supplements, the related yields were quite low, and the formation of undesired products could not be avoided, which was ascribed to catalyst inactivation *via* product accumulation on active sites. Another way to overcome this issue is the utilization of NH_3 and carbon-containing compounds as sacrificial molecules.

DeNO$_x$ via NH$_3$(g) oxidation. The photo-assisted SCR (photo-SCR) of NO(g) with NH_3(g) is an effective way to return N_2 to the atmosphere ($4NO + 4NH_3 + O_2 \rightarrow 4N_2 + 6H_2O$). Back in 1992, Cant *et al.* reported photo-SCR based on the reaction of NO with NH_3 over TiO_2 under UV light irradiation and used isotope labeling to elucidate the reaction pathway ($4^{14}NO + 4^{15}NH_3 + O_2 \rightarrow 4^{14}N^{15}N + 6H_2O$).[107] In this system, NO removal was very slow, and N_2O and NO_3^- were still formed; moreover, the experiment was conducted under unrealistic conditions. Over

Table 2 Performances of various materials as photocatalysts for the denitrification of airborne NO_x

No.	Photocatalyst	Target (Conc.)	Light	Temp.	Flow rate & GHSV	Carrier gas	Supplements	NO conversion (%)	N_2 selectivity (%)	By-products	Ref.
1	TiO_2	NO (1000 ppb)	UV	r.t.	1 L min^{-1}	Air	None	~50	—	NO_2, NO_3^-	96
2	Fe-doped TiO_2					Air		~6	~50	NO_2, NO_3^-	
3						N_2		~4.5	~100	NO_2, NO_3^-	
4	g-C_3N_4	NO (600 ppb)	Visible (420 nm ≤)	r.t.	1 L min^{-1}	Air	None	~38	—	NO_2, undefined	98
5		NO (1500 ppb)				Ar		Almost negligible	—	—	
6	g-C_3N_4 with carbon vacancies	NO (600 ppb)				Air		~48	—	NO_2, undefined	
7		NO (1500 ppb)				Ar		~34	~66	NO_2	
8	Cu^+-ZSM-5	NO (2 Torr)	UV (280 nm <)	r.t.	—	—	None	~2 (4 h)	~100	—	99
9	Ti-MCM-41	NO (180 μmol Eg-cat^{-1})	UV (240 nm <)	r.t.	—	—	None	~1.1 (1 h)	~75	N_2O, undefined	103
10	JCR-TiO_2 (anatase)	NO (1000 ppm)	UV	r.t.	GHSV 32 000 h^{-1}	2% O_2, 98% Ar	NH_3 (1000 ppm)	41	100	—	108
11	JCR-TiO_2 (rutile)							53	100	—	
12	JCR-TiO_2 (anatase 91.3% + rutile 8.7%)							63	100	—	
13	V_2O_5/TiO_2 (1 wt%)	NO (1000 ppm)	UV	r.t.	GHSV 50 000 h^{-1}	2% O_2, 98% Ar	NH_3 (1000 ppm)	17.7	100	—	114
14	CrO_6/TiO_2 (1 wt%)							34.2	100	—	
15	MnO/TiO_2 (1 wt%)							12.1	100	—	
16	Fe_2O_3/TiO_2 (1 wt%)							29.6	100	—	
17	CoO/TiO_2 (1 wt%)							21.6	100	—	
18	NiO/TiO_2 (1 wt%)							27.0	100	—	
19	CuO/TiO_2 (1 wt%)							26.1	100	—	
20	ZnO/TiO_2 (1 wt%)							46.6	100	—	
21	Y_2O_3/TiO_2 (1 wt%)							47.0	100	—	
22	ZrO_2/TiO_2 (1 wt%)							41.1	100	—	
23	Nb_2O_5/TiO_2 (1 wt%)							58.4	>99	—	
24	MoO_3/TiO_2 (1 wt%)							60.2	>99	—	
25	Ta_2O_3/TiO_2 (1 wt%)							38.6	100	—	
26	WO_3/TiO_2 (1 wt%)							63.6	>99	—	
27	N3-dye TiO_2	NO (1000 ppm)	Visible (420 nm ≤)	r.t.	GHSV 100 000 h^{-1}	2% O_2, 98% He	NH_3 (1000 ppm)	>99	>99	—	121
28	$LaFe_{0.4}Mn_{0.6}O_3$/attapulgite	NO (1000 ppm)	UV	r.t.	GHSV 50 000 h^{-1}	3% O_2, 97% N_2	NH_3 (1000 ppm)	~85	~100	—	122
29	$La_{0.7}Ce_{0.3}FeO_3$/attapulgite	NO (1000 ppm)	UV	r.t.	0.1 L min^{-1}	3% O_2, 97% N_2	NH_3 (1000 ppm)	~80	—	—	123
30	$LaFe_{0.5}Ni_{0.5}O_3$/palygorskite	NO (1000 ppm)	Visible (420 nm ≤)	200 °C	GHSV 50 000 h^{-1}	3% O_2, 97% N_2	NH_3 (1000 ppm)	~92	~98	—	124
31	$La_{0.5}Pr_{0.5}CoO_3$/palygorskite	NO (1000 ppm)	Visible (420 nm ≤)	200 °C	GHSV 40 000 h^{-1}	3% O_2, 97% N_2	NH_3 (1000 ppm)	~95	~99	—	125
32	N-doped carbon quantum dot-	NO (1000 ppm)	Visible	150–200 °C	GHSV 50 000 h^{-1}	3% O_2, 97% N_2	NH_3 (1000 ppm)	~93	100	—	127

Table 2 (*Contd.*)

No.	Photocatalyst	Target (Conc.)	Light	Temp.	Flow rate & GHSV	Carrier gas	Supplements	NO conversion (%)	N_2 selectivity (%)	By-products	Ref.
	modified $PrFeO_3$/palygorskite										
33	Fe_2O_3/$SmFeO_3$/palygorskite	NO (1000 ppm)	UV	<200 °C	GHSV 40 000 h^{-1}	3% O_2, 97% N_2	NH_3 (1000 ppm)	~95	100	—	128
34	$LaCoO_3$/appapulgite/rGO	NO (1000 ppm)	UV	100–150 °C	GHSV 50 000 h^{-1}	3% O_2, 97% N_2	NH_3 (1000 ppm)	~95	100	—	129
35	Ag/TiO_2 (1 wt%)	NO (909 ppm)	UV	r.t.	5.5 cm^3 min^{-1}	Ar	CO (1818 ppm)	~35 μmol h^{-1} g^{-1}_{cat}	90	—	136
36	Ag/TiO_2 (5 wt%)							~10 μmol h^{-1} g^{-1}_{cat}	100	—	
37	TiO_2	NO (3000 ppm)	UV	150 °C	—	5% O_2, 3% H_2O in N_2	Carbon black	97	99	N_2O	150

Table 3 Proposed mechanism for the conversion of NO on pristine and Fe-doped TiO_2.[96]

Byproduct (*i.e.*, NO_2 and NO_3^-) formation over TiO_2	
[Reductive pathway]	[Oxidative pathway]
Superoxide radical-mediated	Hydroxyl radical-mediated
$Ti(O_2)_{ads} + e^- \rightarrow Ti(O_2^-)_{ads}$	$Ti{-}OH^- + h^+ \rightarrow Ti{-}OH^•$
$Ti(O_2^-)_{ads} + NO(g) \rightarrow Ti(NO_3^-)_{ads}$	$Ti{-}OH^• + NO(g) \rightarrow Ti{-}H + NO_2(g)$
$Ti(O_2)_{ads} + Ti{-}OH^- + h\nu + 2NO(g) \rightarrow Ti(NO_3^-)_{ads} + Ti{-}H + NO_2(g)$	
[a]Conversion of NO to N_2 over Fe-doped TiO_2	
[Reductive pathway]	[Oxidative pathway]
$V^•_{O(surf)} + 2e^- + NO(g) \rightarrow O_{surf} - N$ (1)	$V_O^x + 2h^+ \rightarrow V_O^{••}$ (4)
$2O_{surf}{-}N \rightarrow 2O_{surf} + N_2(g)$ (2)	
$2O_{surf} \rightarrow O_2(g)$ (3)	
$2NO(g) + 4h\nu \rightarrow N_2(g) + O_2(g)$	

[a] Numbers 1–4 denote the reaction pathway numbered in the scheme of Fig. 7c. $V_O^{••}$ and V_O^x denote charged and neutral oxygen vacancies, respectively.

the past 20 years, Tanaka's group systematically investigated the photo-SCR of NO, mainly focusing on the synthesis of TiO_2-based photocatalysts, reaction mechanism verification, and the design of flow-type photoreactors operable at high gas hourly space velocities (GHSVs).[108,109] From a mechanistic point of view, the photo-SCR of NO over TiO_2 photocatalysts is suggested to comprise five steps (Fig. 9a).[110,111] According to this mechanism, NH_3(g) is adsorbed on the Lewis-acidic sites of TiO_2 (step 1) and is then oxidized by a photogenerated hole (step 2), while the photogenerated electron is trapped by Ti^{4+}. The adsorbed $NH_2^•$ reacts with NO(g) through the Eley–Rideal mechanism (step 3), and the nitrosoamide (NH_2NO) formed as an intermediate decomposes into N_2 and H_2O (step 4). The remaining Ti^{3+} is oxidized by electron transfer to O_2(g) to regenerate Ti^{4+} (step 5). As NH_3 adsorption takes place on Lewis-acidic sites, surface acidity control is an effective way of improving photo-SCR performance, whereas non-acidic surface area and the crystal phase do not contribute to activity enhancement.[112] The rate-limiting step is affected by the concentration of O_2, corresponding to step 4 in the presence of excess O_2 and step 5 at O_2 contents of <2 vol%. Ji *et al.*[113] suggested that (i) the adsorption of NH_3 and its direct oxidation by photogenerated holes was preferred to the dissociative adsorption of NH_3 on TiO_2, as proton-coupled hole transfer was energetically favored ($NH_3 + h^+ + O_{2f}^- \rightarrow NH_2^• + O_{2f}H^-$; O_{2f} denotes a two-fold coordinated O atom in TiO_2) and the formation of NH_2NO proceeded *via* the Eley–Rideal mechanism, and (ii) the decomposition of NH_2NO into N_2 and O_2 was initiated by the transfer of H_b to the O atom, which was followed by either the transfer of H_a to O–H_b or the transfer of O–H_b to the surface Ti atom (Fig. 9b). Step 4 was calculated to have the highest energy barrier among other steps (*i.e.*, it was the rate-limiting step), in line with the experimental result of Tanaka's group.

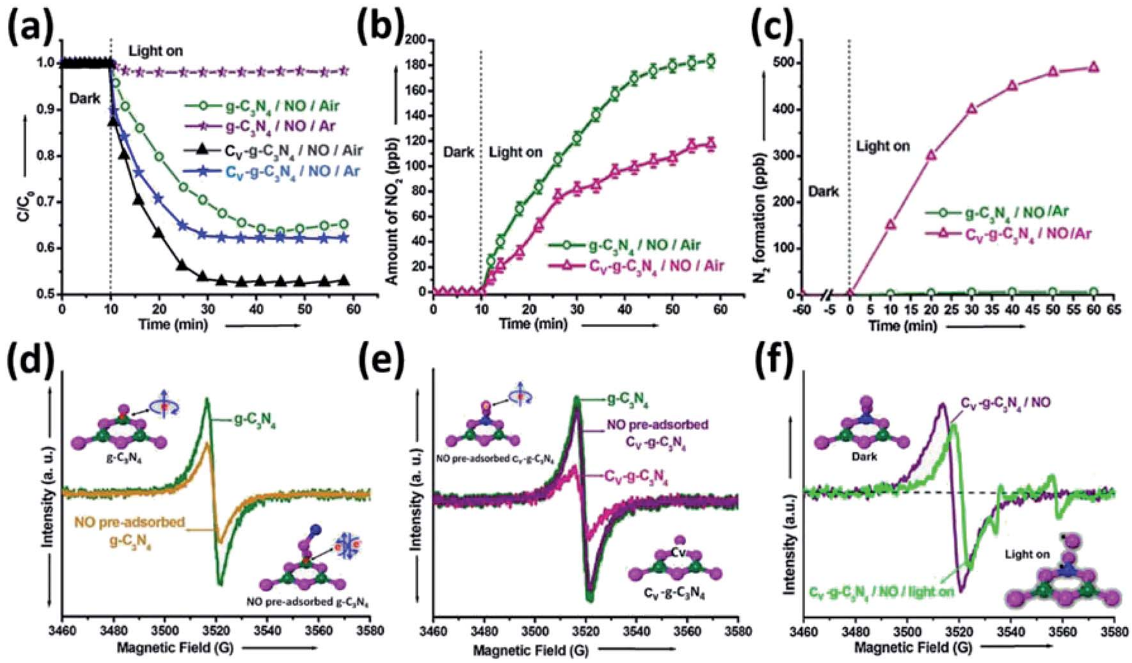

Fig. 8 (a) Photocatalytic removal of NO ([NO] = 1500 ppb) in air and argon over g-C_3N_4 and C_v-g-C_3N_4 under UV light irradiation. Production of (b) NO_2 in air and (c) N_2 in argon over g-C_3N_4 and C_v-g-C_3N_4. ESR spectra of (d) g-C_3N_4 and (e) C_v-g-C_3N_4 before and after NO adsorption. (f) ESR spectra of C_v-g-C_3N_4 with adsorbed NO recorded in the dark and under UV light irradiation. Reprinted with permission from ref. 98. Copyright© 2017, Elsevier.

To realize high catalytic performance or to run the system under visible light, one should appropriately design or modify the photocatalysts. Herein, photocatalysts were classified as those based on TiO_2 or other materials. When TiO_2 was modified with transition metal (V, Cr, Mn, Fe, Co, Ni, Cu, Zn, Y, Zr, Nb, Ta, and W) oxides, increased NO conversion was observed only for the more acidic ZnO, Y_2O_3, Nb_2O_5, MoO_3, and WO_3 (Fig. 10a and Table 2).[114] The low activity observed for other oxides was ascribed to their non-photocatalytic nature or the instability of active sites. The highest activity of WO_3/TiO_2 was attributed to the facile decomposition of NH_2NO on the weakly Lewis-acidic sites of WO_3.[115] The doping of Si into TiO_2 caused the formation of smaller crystals with a higher surface area and pore volume, and acidity was enhanced because of the increased concentration of surface hydroxyl groups.[116] The morphology of TiO_2 was tailored by Ti foil anodization, and high-aspect-ratio TiO_2 nanotubes provided more sites for NH_3 adsorption than spherical TiO_2 (P25).[117] Although TiO_2 does not absorb visible light, the adsorption of NH_3 on TiO_2 could generate an extra energy level in the bandgap *via in situ* doping to induce direct electron transfer from the N 2p orbital to the Ti 3d orbital under irradiation with visible light ($\lambda \geq 400$ nm).[118] This concept resembles that of ligand-to-metal charge transfer.[119] Dye sensitization is an effective way to inject electrons from dye molecules into the conduction band of TiO_2 under visible light. Among the 15 dyes anchored on TiO_2, the Ru(2,2′-bipyridyl-4,4′-dicarboxylic acid)$_2$(NCS)$_2$ complex (N3-dye) showed the highest performance (Fig. 10b).[120,121] The remaining holes in the HOMOs of dye molecules activated NH_3, and N_2 was selectively formed by the reaction between NO_2^- and $NH_2^{\bullet}$. Consequently, the complete conversion of NO and a 100% selectivity for N_2 were achieved at a high GHSV of 100 000 h^{-1} under 30 min irradiation with visible light (Table 2). One of the serious problems of dye-sensitized systems in aqueous media is the detachment of dye molecules from TiO_2 and the dependence of charge transfer on the complexation between functional groups. However, the occurrence of the reaction at the gas–solid interface allows dye desorption to be ignored. Therefore, numerous dyes are available for dye-sensitized SCR.

Yao's group designed diverse types of photocatalytic systems for the photo-SCR of NO, mainly those relying on (i) cascadal electron transfer [$LaFe_{1-x}Mn_xO_3$/palygorskite,[122] $La_{1-x}Ce_xFeO_3$/palygorskite,[123] $LaFe_{1-x}Ni_xO_3$/palygorskite,[124] $La_{1-x}Pr_xCoO_3$/palygorskite,[125] $CaTi_{1-x}Mn_xO_{3-\delta}$[126]], (ii) *Z*-scheme electron transfer [N-doped carbon quantum dots/$PrFeO_3$,[127] Fe_2O_3/$SmFeO_3$/palygorskite,[128] $LaCoO_3$/palygorskite/reduced graphene oxide,[129] $Pr_{1-x}Ce_xFeO_3$/palygorskite,[130] $CeVO_4$/modified palygorskite[131]], and (iii) up-conversion (near-infrared light → UV and visible light) [CeO_2/Pr^{3+}/palygorskite[132] and CeO_2/palygorskite[133]] (Fig. 11 and Table 2). The metal ion content and hetero-element doping in mixed oxides altered the photocatalyst's physical properties such as particle size, electronic band structure, surface acidity, and charge trapping sites, and the supports (palygorskite) were shown to prevent nanoparticle agglomeration and provide sites for NH_3 adsorption. High NO conversion and the selective formation of N_2 were achieved, and the mechanism of NO conversion to N_2 was the same as that reported by Tanaka's group despite the difference in electron transfer pathways proposed. The Ag nano- and sub-nano-clusters incorporated in zeolites also promoted photo-assisted

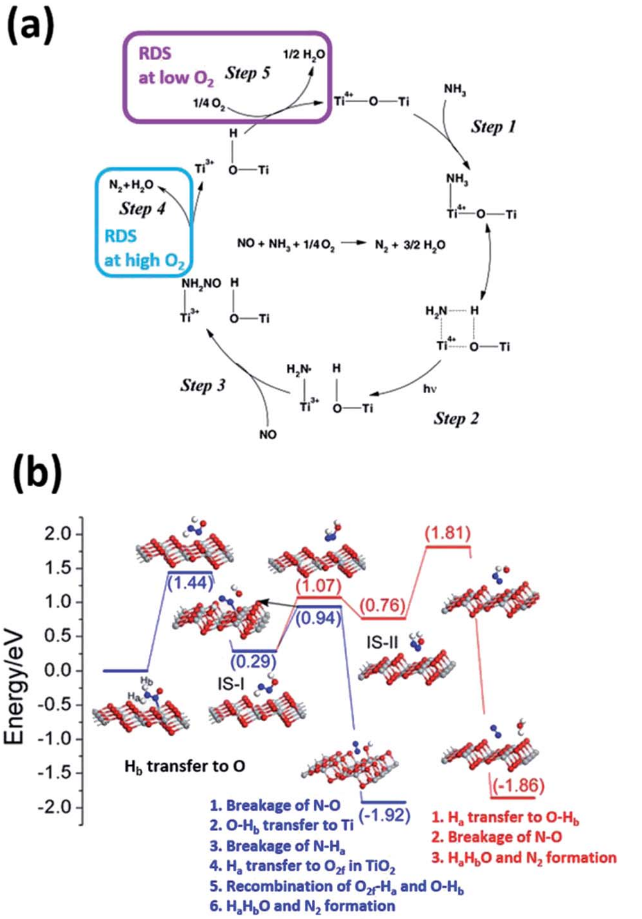

Fig. 9 (a) Mechanism of the photocatalytic reduction of NO by NH_3 over TiO_2. Reprinted with permission from ref. 111. Copyright© 2004, Elsevier. (b) Potential energy diagram for the decomposition of NH_2NO on the (101) surface of anatase TiO_2. Reprinted with permission from ref. 113. Copyright© 2014, American Chemical Society.

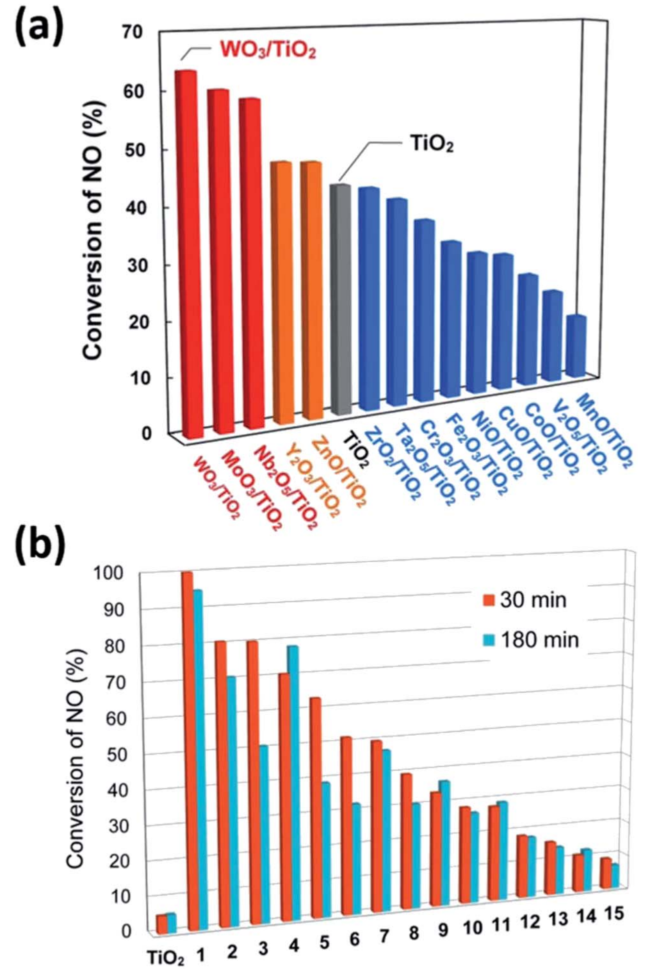

Fig. 10 (a) Photo-SCR of NO over various metal oxide (1.0 wt%)-promoted TiO_2 (GHSV: 50 000 h^{-1}). (b) Photo-SCR of NO over dye-modified TiO_2 under visible light irradiation (dye loading: 12.5 μmol g^{-1}, GHSV: 100 000 h^{-1}). (1) N3 dye, (2) Rose Bengal, (3) eosin Y, (4) $Ru(bpy)_3Cl_2$, (5) rhodamine B, (6) coumarin 343, (7) TCPP, (8) methylene blue, (9) Zn phthalocyanine, (10) Congo Red, (11) phthalocyanine, (12) $RhCl_3$, (13) Indigo Carmine, (14) Cu phthalocyanine, and (15) carmine dyes. Reprinted with permission from ref. 109 and 121. Copyright© 2016 and 2015, Wiley.

SCR under visible light irradiation ($\lambda \geq 390$ nm), with activity determined by the reaction temperature (room temperature *vs.* 150 °C).[134] $Ag_n^{\delta+}$ clusters were utilized as sensitizers because of their surface plasmon resonance and they favored the decomposition of NH_2NO to N_2 at 150 °C as opposed to the further oxidation of $NH_2^{\bullet}$ to NO and then to NO_2 by singlet oxygen at room temperature.

DeNO$_x$ via the oxidation of carbon-containing compounds. NH_3 can be replaced by CH_4, C_3H_8, C_4H_{10}, CO, $CO(NH_2)_2$, C_2H_5OH, carbon black, *etc.* for the photo-SCR of NO to N_2 over TiO_2-based catalysts under aerobic conditions. Bowering *et al.* tested the photocatalytic conversion of NO to N_2 over TiO_2 (P25) in the presence of CO as a reducing agent under UV light irradiation and showed that the reaction did not follow the Eley–Rideal mechanism but was rather driven by the adsorbed CO and NO (*i.e.*, (i) $CO_{ads} + O_{ads} \rightarrow CO_2(g)$; (ii) $CO_{ads} + 2NO_{ads} \rightarrow N_2O_{ads} + CO_{2ads}$; (iii) $CO_{ads} + N_2O_{ads} \rightarrow N_2(g) + CO_{2ads}$).[135] Therefore, the rate of NO conversion was the highest under CO-free conditions owing to the absence of competitive adsorption, whereas the highest selectivity for N_2 was achieved in the presence of CO even though NO conversion was reduced. In the latter case, the surface hydroxyl groups significantly influenced selectivity (more hydroxyl groups led to better performance), and the loading of Ag on TiO_2 markedly enhanced selectivity while reducing NO conversion, as Ag clusters acted as centers for electron–hole pair recombination.[136] The electron defects (Ti^{3+}, F^+, and F centers) intentionally introduced on TiO_2 by partial reduction could reduce NO under visible light irradiation, and the presence of CO as a regenerator of donor centers increased the selectivity for N_2.[137] Although extra experiments were also performed in the presence of hydrocarbons such as C_2H_6, C_2H_4, C_3H_8, propylene, C_4H_{10}, benzene, toluene, ethylbenzene, and *o*-xylene, the research goal was not the selective conversion of NO to N_2 but the utilization of NO as an oxidant for the removal of VOC.[138,139]

Wu's group employed photo-SCR for denitrification in the presence of saturated hydrocarbons including CH_4,[140,141]

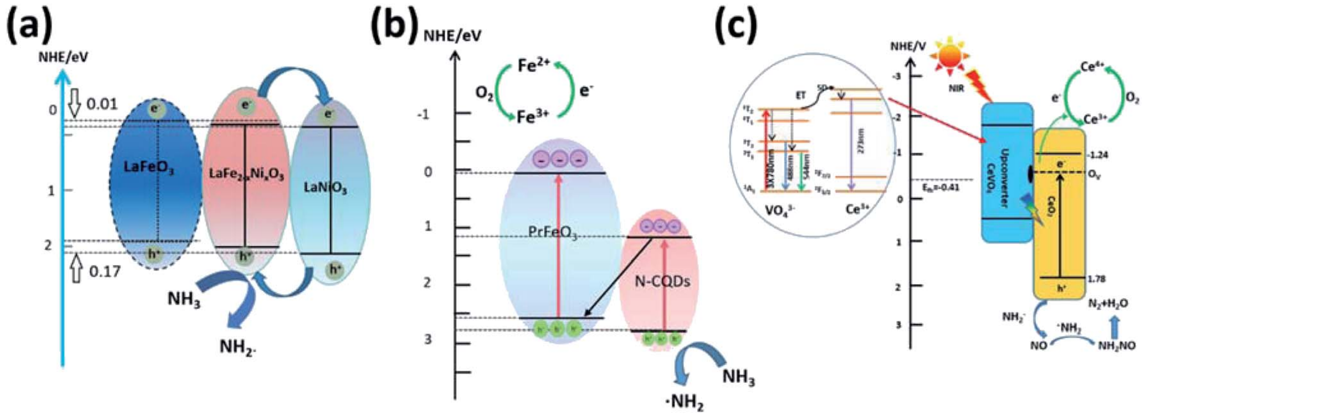

Fig. 11 Schematic diagrams of (a) cascadal electron transfer, (b) *Z*-scheme electron transfer, and (c) electron transfer in composite materials for the photocatalytic oxidation of NH_3. Reprinted with permission from ref. 124 and 133. Copyright© 2018 and 2020, Elsevier. Reprinted with permission from ref. 127. Copyright© 2018, American Chemical Society.

C_3H_8,[142–144] and C_4H_{10} [145–147] as reducing agents, focusing on the synthesis of TiO_2 and its structure/surface modification in Pd/TiO_2, PtO_xPdO_y/TiO_2, PdO/TiO_2, Ag/TiO_2, Cu/TiO_2, Pt/TiO_2, and TiO_2 nanosheets. In the absence of co-catalysts on TiO_2, the electron-donating behavior of hydrocarbons was not effectively utilized, unlike in the case of NH_3. However, the temperature and the presence of moisture and oxygen were important for controlling NO conversion and selectivity for N_2. For example, when PtO_xPdO_y/TiO_2 was tested at temperatures of 25, 70, and 120 °C, the best performance was observed at the highest temperature when either oxygen or water vapor was present, as these conditions helped to avoid the accumulation of nitrate and the desorption of water vapor from active sites, respectively. On the other hand, the opposite trend was observed under vapor- and oxygen-free conditions because of the poor adsorption of C_3H_8 and NO (competitive adsorption as in the case of CO) on the catalyst surface at high temperature. Without PtO_xPdO_y catalysts, NO oxidation was dominant, and therefore, nitrate was formed as the major product, with its accumulation on the surface resulting in a decrease of activity with reaction time.

The utilization of urea, C_2H_5OH, and carbon black as reducing agents was also possible for the photocatalytic denitrification of NO to N_2. In the case of TiO_2 and urea co-supported carbon fiber, TiO_2 and urea promoted the formation of NO_2 and the sequential reduction of NO_2 to N_2 at room temperature, respectively, with moisture accelerating the desorption of NO_2 from TiO_2.[148] In the case of Au/TiO_2 + ethanol, the adsorption and dissociation of ethanol on Au particles or at the Au/TiO_2 interface initiated the reaction at room temperature when $C_2H_5O_{ads}$ accepted a photogenerated electron. This reaction was also promoted by the by-products (CH_3CHO, H_2, CO, and CH_4) formed by ethanol decomposition.[149] Last, the reduction of NO to N_2 was conducted over TiO_2 along with the photocatalytic oxidation of carbon black to CO_2 in the presence of O_2 and moisture at 150 °C, providing the possibility of utilizing solid materials as reductants (Table 2).[150]

2.2.2. Photocatalytic removal of N_2O(g) to N_2. Several decades ago, the photocatalytic denitrification of N_2O to N_2 was investigated on ZnO at 371–431 °C under UV light irradiation, which induced the decomposition of N_2O *via* a combination of thermocatalysis and photocatalysis.[151] The thermocatalytic reaction followed first-order kinetics, while the photocatalytic reaction kinetics was more complicated and governed by N_2O^- that was formed as an intermediate through electron transfer from ZnO to N_2O. The mechanism proposed for n-type metal oxides in the dark at 20 °C comprises five steps and features step 2 as the rate-limiting step and $O_{ads}^- \cdots MO^+(s)$ as the dominant species because of the fast dissociation of $N_2O_{ads}^-$ (Fig. 12a).[152] Therefore, the N_2 formation rate sharply increased and then saturated within the initial reaction stage over ZnO, in which case the kinetics was much faster than in the case of the photocatalytic reaction (Fig. 12b). Although the quantum efficiency of photo-assisted dissociation was small, an additional increase in N_2 generation clearly appeared with time, and the reaction pathway (*i.e.*, $N_2O_{ads} + (e^- + h^+) \rightarrow N_2O^*_{ads} \rightarrow N_2(g) + O_{ads}$) was specified by the migration of photogenerated charge carriers to the surface of ZnO. Electron paramagnetic resonance spectroscopy revealed that electrons are transferred to N_2O_{ads} ($N_2O_{ads} + e^- \rightarrow N_2(g) + O_{ads}^-$), and O_{ads}^- might be localized at oxide ion vacancies *via* migration, while holes can be trapped at oxide ions *via* migration through the lattice.[153] Anpo *et al.* detected hyperfine splitting caused by one nitrogen atom at 77 K, which indicated the formation of either N_2O^- or $N_2O_2^-$ ($N_2O + O^- \rightarrow N_2O_2^-$) on TiO_2 supported by porous Vycor glass.[154,155]

Kudo *et al.* reported the denitrification of N_2O over metal (Pt, Ag, and Cu)-loaded TiO_2 in the presence of electron donors (water or/and methanol vapor) under UV light.[156,157] Pt promoted the separation of electron–hole pairs, the dissociation of N_2O, and the supply of adsorbed hydrogen atoms (*i.e.*, $H^+ + e^- \rightarrow H$; $N_2O + 2H \rightarrow N_2 + H_2O$; $N_2O^- + H \rightarrow N_2 + OH^-$), while water was oxidized on TiO_2 ($4OH^- + 4h^+ \rightarrow O_2 + 2H_2O$). In the presence of both water and CH_3OH vapor, the photocatalytic activity of Pt/TiO_2 for N_2O reduction was almost negligible, as the photogenerated electrons were selectively transferred to

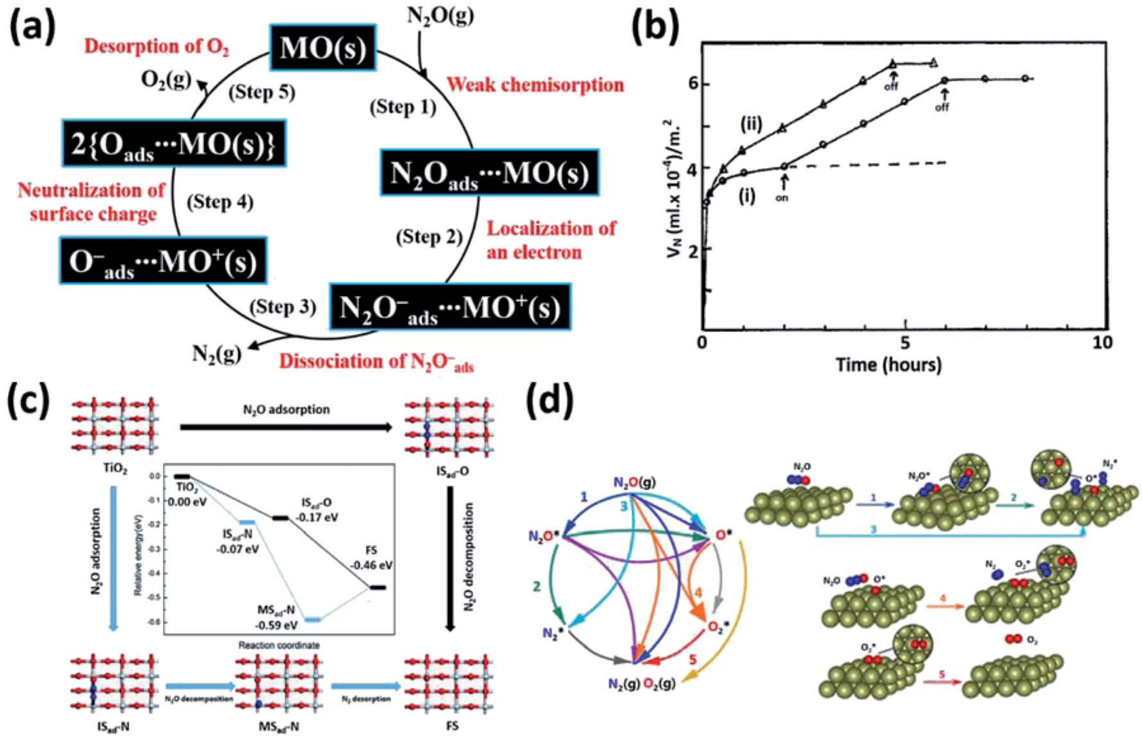

Fig. 12 (a) Mechanism of the conversion of N_2O to N_2 and O_2 over a metal oxide surface. (b) Time-dependent production of N_2 (V_N) from N_2O (10 Torr) over an activated ZnO surface at 20 °C under (i) dark and light on/off conditions indicated by arrows and (ii) continuous illumination. Reprinted with permission from ref. 152. Copyright© 1971, American Chemical Society. (c) Relative energy diagram for the photocatalytic decomposition of N_2O on perfect anatase (001) facets. Reprinted with permission from ref. 173. Copyright© 2018, Royal Society of Chemistry. (d) Reaction diagram for the conversion of N_2O to various adsorption and decomposition products (N_2O^*, N_2^*, O^*, O_2^*, N_2(g) and O_2(g); * designates adsorbed species). (1–3) Dissociative adsorption of N_2O on Ir(111), (4) formation of surface peroxides, and (5) O_2 desorption from Ir(111). Reprinted with permission from ref. 177. Copyright© 2019, American Chemical Society.

water to produce H_2. Ag- and Cu-loaded TiO_2 promoted denitrification, probably because of the facile dissociation of N_2O_{ads} on Au and Cu surfaces as well as the relatively high kinetic barrier for the reduction of water by electrons. Sano *et al.* further probed the removal of N_2O over Ag/TiO_2 in the presence of CH_3OH vapor and showed that the photocatalytic performance was affected by the oxidation state of Ag.[158] In particular, partially reduced Ag_2O prepared by photodeposition was more active than metallic Ag, which was ascribed to Ag^+-mediated charge transfer ($N_2O_{ads} + e^- \rightarrow N_2O^-{}_{ads}$; $N_2O^-{}_{ads} + Ag^+ \rightarrow N_2 +$ Ag–O; 3Ag–O + $CH_3OH_{ads} + 3h^+ \rightarrow 3Ag^+ + CO_2 + 2H_2O$).

Metal ions (Cu^+, Ag^+, Pb^{2+}, and Pr^{3+}) were immobilized on the surface of metal oxides (SiO_2, Al_2O_3, and SiO_2/Al_2O_3) or incorporated inside ZSM-5 zeolite pores to promote the photo-assisted removal of N_2O. Cu^+-anchored metal oxides were prepared by an ion-exchange method with thermovacuum treatment, and linear two-coordinate and planar three-coordinate Cu^+ ions were observed on SiO_2/Al_2O_3 and Al_2O_3 or SiO_2, respectively.[159] In this case, Cu^+ was assumed to undergo a $(3d^{10}),{}^1S_0 \rightarrow (3d)^9(4s)^1,{}^1D_2$ electronic transition under UV light irradiation, and electron transfer from the photo-excited Cu^+ to N_2O initiated denitrification. Photocatalytic activity was affected by the coordination geometry (linear or planar) and the aggregation state (isolated Cu^+ monomer or Cu^+–Cu^+ dimer) of Cu^+ and was the highest for the isolated linearly coordinated Cu^+ monomer owing to the long lifetime of charge carriers coupled with the low accumulation of O_{ads} due to O_2 release. As Cu^+ was incorporated in ZSM-5 and Y zeolite cavities, the type of Cu^+ species depended on the degassing temperature, which suggested that the excited state of the Cu^+–Cu^+ dimer was an effective N_2O quencher.[160–162] In the case of Ag^+-exchanged ZSM5, UV light irradiation induced the $4d^{10} \rightarrow 4d^95s^1$ transition of two-coordinate isolated Ag^+ ions, and the complexation of Ag^+ with N_2O provided a channel for electron transfer from the excited Ag^+ to the antibonding molecular orbital of N_2O.[163] For Pb^{2+}-exchanged and Pr^{3+}-supported catalysts, the reaction mechanisms were similar to those observed for Cu^+- and Ag^+-exchanged ones.[164,165]

Kočí's group reported diverse photocatalysts for the decomposition of N_2O under UV light irradiation, *e.g.*, ZnS/montmorillonite,[166] cordierite/steatite/CeO_2,[167] TiO_2/C_3N_4,[168] WO_3/C_3N_4,[169] ZnO/C_3N_4,[170] $BiOIO_3/C_3N_4$,[171] and $BiVO_4/C_3N_4$.[172] Among them, binary photocatalyst combinations helped to inhibit charge carrier recombination and therefore exhibited enhanced photocatalytic denitrification performances. Although some of these photocatalysts exhibited visible-light activity, all experiments were carried out under UV light. Moreover, the physicochemical interactions between the catalyst surface and N_2O were not deeply investigated. To bridge this gap, Liu's group used DFT calculations to model the decomposition of N_2O on TiO_2,[173] CeO_2,[174] $BiVO_4$,[175,176] $BiMoO_6$,[176] and Bi_2WO_6,[176] obtaining results well correlated with experimental findings. For example, in the case of TiO_2, the photogenerated electrons did not affect N_2O adsorption, but the presence of oxygen vacancies or excited electrons promoted the N_2O decomposition reaction. The surface-trapped electrons at five-coordinate Ti ($Ti_{5c}^{4+} + e^- \rightarrow Ti_{5c}^{3+}$) centers could act as active sites for N–O bond cleavage, with the reaction pathway depending on the adsorption geometry, *i.e.*, on whether N_2O ($O{=}N^+{=}N^- \leftrightarrow {}^-O{-}N^+{\equiv}N$) was adsorbed on TiO_2 *via* the oxygen or the nitrogen end. In the case of decomposition on perfect anatase (001) facets, the N_2O adsorbed on Ti^{3+} *via* the oxygen end possessed an exothermic energy of 0.17 eV, and the O–N bond cleavage by the transfer of excited electrons from Ti^{3+} to N_2O featured an exothermicity of 0.29 eV and produced N_2 (Fig. 12c). On the other hand, the N_2O adsorbed on Ti^{3+} *via* the nitrogen end formed an intermediate bridging configuration (with a binding energy of 0.19 eV), and the N–O bond cleavage was characterized by an enthalpy change of −0.40 eV. Finally, N_2 release from TiO_2 was an endothermic (by 0.13 eV) process. The removal of O^- was ascribed to O^- discharge followed by recombination with another O atom, which proceeded *via* hole transfer to O^- and could decrease the energy barrier for O_2 production.

An Al–Ir plasmonic antenna reactor combining plasmonic metallic antenna nanoparticles (Al nanocrystals) with nearby catalytic reactors (Ir nanoparticles) was designed for the photocatalytic conversion of N_2O to N_2 and O_2.[177] At high GHSVs (≥80 000 h^{-1}), the conversion efficiency reached 10%, and N_2 and O_2 were the only products formed. The apparent activation energy was maintained irrespective of illumination, which suggested that photothermal heating rather than hot carriers generated by the plasmon effect was responsible for N_2O decomposition. As depicted in Fig. 12d, the pre-adsorption of N_2O on Ir (step 1) and the dissociation of N_2O (step 2) are not necessary because of the high exothermicity of the dissociative adsorption of $N_2O(g)$ into N_2^* and O* at high operating temperatures (step 3). For fully saturated O*, the direct interaction between $N_2O(g)$ and O* can be driven by the Eley–Rideal mechanism to produce surface peroxide (step 4, moderately endothermic). Finally, the reaction is completed by the highly endothermic desorption of surface peroxide (O_2^*; step 5), which was assumed to be the rate-limiting step for the overall N_2O decomposition on Ir(111).

3. Oxidation of ammonia to N_2 under aerobic and anaerobic conditions

Ammonia is one of the most valuable chemicals in agricultural and other industries, and has recently received much attention as a hydrogen carrier.[178] As the manufacture of NH_3 by the Haber–Bosch process is highly energy-intensive and consumes H_2 that is mainly derived from fossil fuels, the economically feasible utilization of NH_3 as a hydrogen carrier requires the development of highly active catalysts for the production of NH_3 and its decomposition to H_2 under mild conditions.[179,180] Therefore, much effort has been directed at the establishment of new methods of ambient-condition N_2 fixation, particularly those using renewable energy resources.[181] Among these methods, the photocatalytic reduction of N_2 to NH_3 holds great promise, as the electrons and hydrogen are provided by sunlight and water, respectively, although the cleavage of the N≡N bond in N_2 at standard temperature and pressure is a big challenge because of the low solubility of this gas.[182] From an environmental perspective, NH_3 is not a useful chemical but a pollutant because of its high toxicity, corrosivity, odor, *etc.*, and should therefore be effectively removed from air and water. The expansion of agricultural infrastructure to satisfy the increasing global food demand is facilitating the release of NH_3 (from fertilizers, livestock excretions, *etc.*) to the atmosphere and water bodies.[183] Most studies on photocatalysis target the oxidation of NH_3 to N_2 or NO_x ($2NH_3 + 1.5O_2 \rightarrow N_2 + 3H_2O$, $\Delta_r G^0_{298} = -652.41$ kJ mol^{-1}; $2NH_3 + 4O_2 \rightarrow 2HNO_3 + 2H_2O$, $\Delta_r G^0_{298} = -585.4$ kJ mol^{-1}), with comprehensive catalysts and relevant reaction mechanisms summarized in recent reviews.[184,185] Herein, we briefly describe the photocatalytic decomposition of NH_3 on TiO_2 and present several examples of relatively high performance for the selective conversion of NH_3 to N_2 at room temperature.

Fig. 13a presents the mechanism of the photocatalytic oxidation of gas-phase NH_3 on Pt/TiO_2 in the presence/absence of water vapor under anaerobic conditions.[186] Initially, NH_3 is adsorbed on both Lewis- and Bronsted-acidic sites of TiO_2 (mainly hydroxyl groups), and the reaction is initiated by the charge carriers generated under UV light irradiation. The electrons migrate to Pt nanoparticles to reduce protons and thus produce H_2. The oxidation of adsorbed NH_3 occurs *via* hole transfer, and the coupling of two amide radicals ($NH_2^\bullet$) produces N_2H_4, which can be subsequently converted into H_2 and N_2H_2. Finally, N_2H_2 self-decomposes into N_2 and H_2 or disproportionates into N_2 and N_2H_4. As this process does not involve the formation of NO_x, the $H_2 : N_2$ molar ratio was recorded as 2.9, which was close to the theoretical value of 3.0 for the decomposition of NH_3 to N_2 and H_2. Although the hole-mediated oxidation of $NH_2^\bullet$ to N through NH to release N_2 is also possible, it is energetically unfavorable because of its higher net activation energy.[160] Under dry conditions, the accumulation of NH_4^+ ions on TiO_2 promotes catalyst deactivation, as these ions cannot easily migrate to Pt nanoparticles in the absence of water (Fig. 13b).

When TiO_2 is used under aerobic and humid conditions, various nitrogen-containing species (*e.g.*, NO, NO_2, NO_2^-, NO_3, NO_3^-, N_2O, HONO, and N_2H_4) might be involved as intermediates or produced as by-products during NH_3 oxidation,[188–194] which complicates the selective production of N_2. When the experiment was carried out by irradiating TiO_2 in a flow tube with a stream of NH_3-containing air, HONO was formed as an intermediate.[190] The production of HONO was negligible in the absence of O_2 and exhibited a volcano-type dependence on the concentration of NH_3. The increase in [HONO] was ascribed to the photoreduction of NO_2 ($NH_3 \rightarrow NO_2 \rightarrow$ HONO), while the decrease in [HONO] at higher NH_3 concentrations was ascribed to the saturation of surface-active sites according to the

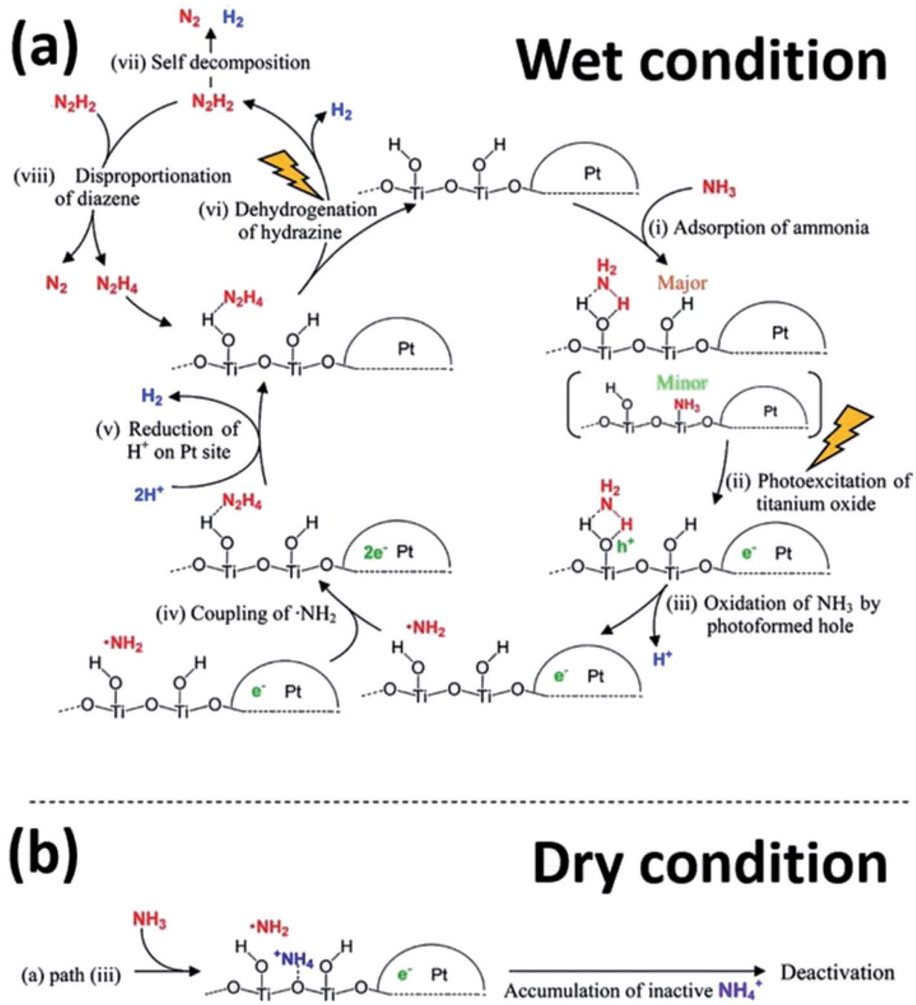

Fig. 13 Proposed mechanism of the photocatalytic decomposition of NH_3 on Pt/TiO_2 in the (a) presence and (b) absence of water. Reprinted with permission from ref. 186. Copyright© 2012, American Chemical Society.

Langmuir–Hinshelwood model and the reaction with NH_3 ($NH_3 + HONO \rightarrow NH_4NO_2 \rightarrow N_2 + 2H_2O$). In a similar manner, [HONO] exhibited a volcano-like dependence on the relative humidity of the gas flow. Water accelerated the formation of HONO at low humidity, although excess water could occupy the pores of TiO_2, hinder the access of NH_3 to active sites, and facilitate the quenching of $OH^•$ to decrease [HONO]. In this experiment, NO_x was formed as the major by-product. Instead of probing the complete conversion of NH_3 to N_2, almost all studies investigated the photocatalytic abatement of NH_3 without analyzing the composition of the final products.

As mentioned earlier, the selective conversion of gaseous NH_3 to N_2 under aerobic conditions is challenging. From a practical viewpoint, operation under anaerobic conditions does not make sense, as the photocatalytic process is designed to remove few-ppm-level NH_3 from air. In this regard, an anammox-like process aims to completely remove nitrogen species from aqueous systems (mainly NH_3-containing wastewater) or use concentrated NH_3 solutions as hydrogen carriers to provide H_2 for fuel cells and should be more feasible owing to the ease of inert atmosphere generation *via* N_2 or Ar purging. The protonation of NH_3 ($pK_a \approx 9.25$) and the positive change of TiO_2 surface charge (pH_{zpc} 6–7 for P25) in acidic and neutral media cause electrostatic repulsion (*i.e.*, $NH_4^+ \leftrightarrow$ >Ti–OH_2^+), which hinders the adsorption of NH_4^+ and inhibits the photocatalytic reaction.[195] Moreover, whereas NH_4^+ is stable against attack by $OH^•$, neutral NH_3 is degraded by $OH^•$ under photocatalytic conditions.[196–198] Therefore, high photocatalytic performance was achieved at pH 10–11, whereas an activity decrease was observed at higher pH, probably because of the low solubility of NH_3 under these conditions.

The use of metal nanoparticles as co-catalysts offers a simple way to increase the yield and selectivity of photocatalytic processes, prolong charge carrier lifetime, and provide catalytically active sites. Among the various metal nanoparticles used in conjunction with TiO_2, Pt nanoparticles exhibited an outstanding performance for the decomposition of NH_3 into N_2 and H_2 under both oxic and anoxic conditions.[199–201] Based on the calculated adsorption energies, Pt (−394 kJ mol^{-1}) has a moderate atomic nitrogen affinity for N_2 formation among the tested metals (*e.g.*, Ag (−156 kJ mol^{-1}), Au (−162 kJ mol^{-1}), Rh (−448 kJ mol^{-1}), Ru (−525 kJ mol^{-1})).[202] In comparison with bare TiO_2, which generated only nitrite and nitrate as end-products under air-saturated conditions, the loading of Pt (0.2 wt%) accelerated the reaction kinetics and promoted the evolution of N_2 to reduce the total N content in the NH_3 solution.[170] Interestingly, the presence of O_2 had little influence on the kinetics over Pt/TiO_2, for which the efficiency of the NH_3 to N_2 conversion after 2 h irradiation equaled 65–70% in both air and N_2. Pt nanoparticles on TiO_2 probably stabilized NH_x species generated as intermediates by $OH^{\bullet}$-mediated chain reactions. When O_2 was replaced by N_2O, more OH radicals were formed through the reductive dissociation of N_2O on Pt to increase the efficiency of the NH_3 to N_2 conversion to 80%. The photocatalytic conversion of NH_3 and the selectivity for N_2 simultaneously increased with the increase in the loading of Pt on TNTs under oxic conditions. In particular, an ammonia conversion of 100% (for $[NH_3]_i = 20$ ppm) and a selectivity of 87.5% were achieved after 3 h irradiation for Pt/TNTs (25 wt% Pt).[200] Although the reductive dissociation of NH_3 on Pt and the overoxidation of NH_3 on TNTs might be responsible for the formation of N_2 and NO_x ions, respectively, it is still unclear whether the reductive dissociation of NH_3 is energetically favorable or not, and the function of nitrogen hydrogen radicals on Pt as electron/hole recombination centers remains to be explored.

Under anaerobic conditions, the $H_2 : N_2$ molar ratio achieved at alkaline pH using metallized photocatalysts (Pt/TiO_2, Pt/Fe-doped TiO_2, Ni/TiO_2, $Pt_{0.9}Au_{0.1}/TiO_2$, and Ru/ZnS) was close to the theoretical molar ratio (3 : 1). The main advantage of the anammox-like process is its ability to achieve both the complete removal of NH_3 from wastewater and the recovery of H_2 as a fuel for fuel cells at room temperature under sunlight. For example, in a highly concentrated solution (0.59 M), NH_3 was decomposed at pH 10–12 over Pt/TiO_2 (0.5 wt% Pt) to afford H_2 and N_2 in a 3 : 1 molar ratio, and the catalyst performance was governed by Pt loading, pH, photocatalyst type, and co-catalyst type. Despite the lack of supporting evidence, Pt was assumed to provide active sites for the reduction of protons to H_2, while the oxidation of NH_3 occurred on TiO_2. When Pt/Fe-doped TiO_2 (0.5 wt% Pt and 1.0 wt% Fe) was tested in 0.59 M NH_3 under UV light irradiation, a 3 : 1 (mol/mol) $H_2 : N_2$ ratio was recorded.[203] The higher H_2 yield of Pt/Fe-doped TiO_2 (27 μmol mg_{cat} mol^{-1}) than that of Pt/TiO_2 (18 μmol mg_{cat} mol^{-1}) was due to the better absorption of visible light in the former case. Except for the case of Ni/TiO_2, the loading of non-noble-metals (V, Cr, Mn, Fe, Co, and Cu) on TiO_2 slightly decreased the H_2 yield, whereas the $H_2 : N_2$ molar ratio of 3 : 1 was maintained (0.59 M NH_3).[188] As seen in Fig. 14a, the amounts of

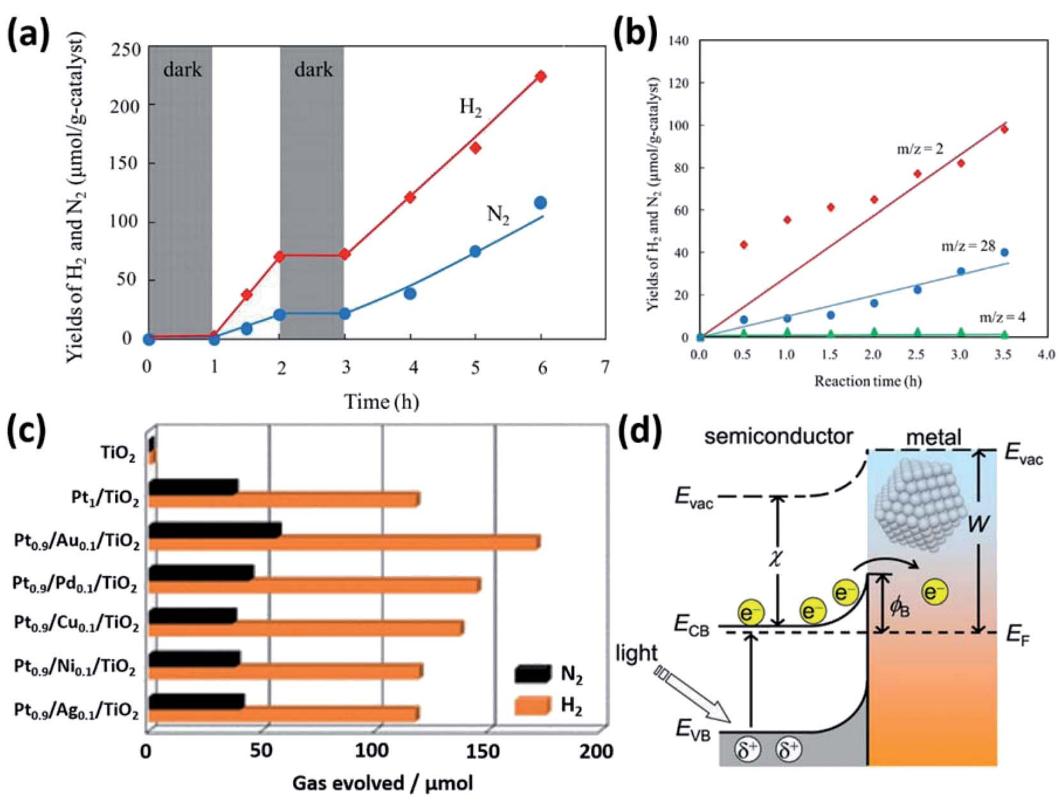

Fig. 14 (a) Time profiles of H_2 and N_2 production by the photodecomposition of NH_3 over Ni/TiO_2 (1.0 wt%) in the dark and under illumination. (b) Time profiles of gas-phase product yields for the photocatalytic decomposition of NH_3 over Ni/TiO_2 in D_2O. Reprinted with permission from ref. 187. Copyright© 2017, Elsevier. (c) Amounts of H_2 and N_2 evolved during the 6 h photocatalytic decomposition of NH_3 on $Pt_{0.9}M_{0.1}/TiO_2$ (M: Au, Pd, Cu, Ni, and Ag, total metal loading on TiO_2: 0.1 mol%). (d) Schematic electronic structure of a metal/semiconductor interface. E_{vac}, E_F, W, φ_B, and χ denote the vacuum level, Fermi energy level, metal work function, Schottky barrier, and the electron affinity of the semiconductor conduction band, respectively. Reprinted with permission from ref. 204. Copyright© 2020, American Chemical Society.

N_2 and H_2 produced over Ni/TiO_2 (0.5 wt% Ni) linearly increased with increasing irradiation time, and the reaction completely stopped in the dark. Isotope labeling experiments performed with D_2O revealed that no D_2 and HD were produced, *i.e.*, the hydrogen in H_2 stemmed from NH_3 and not from water (Fig. 14b). This result indicates that the photodecomposition of NH_3 occurred on the interface between metal nanoparticles and TiO_2 and involved the direct migration of $H^\bullet$ (formed by the hole-mediated reaction of NH_3) to Pt. DFT calculations indicated the existence of two possible pathways for TiO_2-based NH_3 decomposition, namely (i) $2NH_{3,\ ads} \rightarrow 2NH_2^\bullet + H_2(g) \rightarrow H_2N\text{–}NH_2 + H_2(g) \rightarrow {}^\bullet N{=}N^\bullet + 3H_2(g) \rightarrow N_2(g) + 3H_2(g)$ and (ii) $NH_{3,\ ads} + NH_3 \rightarrow NH_2^\bullet + H^\bullet + NH_3 \rightarrow NH_2\text{–}NH_3 + H^\bullet \rightarrow H_2N\text{–}NH_2 + H_2(g) \rightarrow {}^\bullet N{=}N^\bullet + 3H_2(g) \rightarrow N_2(g) + 3H_2(g)$. The formation of NH_2–NH_2 was probably assisted by metallic Ni. The loading of bimetallic alloy nanoparticles on TiO_2 is also a good way to enhance the photocatalytic activity of monometallic nanoparticle/TiO_2 hybrids, with the highest activity obtained for $Pt_{0.9}Au_{0.1}$ under UV light irradiation (Fig. 14c).[204] As depicted in Fig. 14d, charge separation efficiency is determined by the Schottky barrier (φ_B; φ_B = metal work function (W) − electron affinity of the TiO_2 conduction band (χ)). The introduction of Au into Pt reduces φ_B, which was calculated as 1.84, 1.62, and 0.97 eV for Pt/TiO_2, $Pt_{0.9}Au_{0.1}/TiO_2$, and Au/TiO_2, respectively. Overly high and low φ_B values suppress electron separation and promote reverse electron transfer, thus decelerating photocatalytic reactions. The decomposition of NH_3 into N_2 and H_2 was also carried out using other photocatalysts such as RuO_2–NiO–$SrTiO_3$,[205] ZnO,[206] and Ru/ZnS,[207] the activities of which were much lower than that of Pt/TiO_2. The visible light-induced decomposition of NH_3 into N_2 and H_2 was also attempted in a dye-sensitized system comprising a homogeneous tris(bipyridine)ruthenium(II) ($Ru(bpy)_3^{2+}$) dye, methyl viologen as an electron mediator, and O_2 as an electron acceptor.[208] Under visible light irradiation, $Ru(bpy)_3^{3+}$ oxidized NH_3 and was converted to the original state, $Ru(bpy)_3^{2+}$.

4. Photoelectrochemical denitrification and ammonia oxidation

Only a few studies deal with photoelectrochemical denitrification and ammonia oxidation, focusing on the recovery of N_2 from nitrogen species. The photoelectrochemical denitrification of nitrite (1 mM $NaNO_2$ at pH 7) was first achieved in 1999 using a three-electrode system (counter electrode (CE) = Pt wire, reference electrode (RE) = saturated calomel electrode (SCE), and working electrode (WE) = roughened Ag electrode) in 0.1 M Na_2SO_4 as an electrolyte under laser irradiation (362, 413, 457, 476, 488, 496, 514, and 647 nm) and a nitrogen atmosphere.[209] Denitrification was initiated by the excitation of Ag *via* plasmon resonance and the electrochemical current generated at −1.0 V_{SCE}. Notably, irradiation brought about not only an increase in cathodic current but also a positive shift of the onset potential. The quantum efficiency was estimated as 0.04% without the analysis of real-time NO_2^-, NO_3^-, N_2, and NH_3 concentrations. Nitrate reduction was believed to involve the electrochemical nitrate to nitrite conversion followed by the photoelectrochemical reduction of nitrite to NH_3 and N_2. The photoelectrochemical nitrate to nitrite conversion was also observed for Ag nanopyramids (1 M $NaNO_3$ at pH 5.7 under Ar), in which case the plasmon resonance of Ag resulted in an almost 100% faradaic efficiency at −1.0 V_{RHE}.[210]

The photoelectrochemical nitrate to nitrite reduction was also promoted by semiconducting photocathode materials such as *p*-$GaInP_2$, nanoporous *p*-Si, and CuI/PbI_2. In the case of *p*-$GaInP_2$, data were collected in a three-electrode system (CE = Pt black, RE = Ag/AgCl, and WE = *p*-$GaInP_2$) in 0.1 M HNO_3 + 0.5 M NH_4NO_3 as an electrolyte (pH 1) under simulated solar light at an air mass (AM) of 1.5 G.[211] The faradaic efficiency of nitrate reduction was calculated as 80%, and the incident-photon-to-current efficiency (IPCE) at −1.0 $V_{Ag/AgCl}$ was recorded as 100, 60, and 5% under excitation at 400, 580, and 610 nm, respectively. As a close to zero current was obtained in the dark, illumination was concluded to stimulate the rate-limiting step, and the catalytically active sites were assumed to be Ga and/or In. For nanoporous *p*-Si under similar conditions, the faradaic efficiency of nitrate reduction at −0.6 $V_{Ag/AgCl}$ equaled 65%, and no NH_3 and N_2 were observed.[212] In the case of CuI–PbI_2, the faradaic efficiency of nitrate reduction in 0.1 M $NaNO_3$ exceeded 52%, and the IPCE at 400 nm was around 15%.[213] The bubbles evolved on the photoelectrode surface probably contained N_2 rather than H_2, as no H_2 signal was observed by gas chromatography. Interestingly, isotope labeling experiments performed in Ar-saturated 0.1 M $Na^{15}NO_3$ solution (98% ^{15}N) revealed that the generation of NH_3 was due to an external contamination and not nitrate reduction.

n-type semiconductors can be used as photoanodes for the water oxidation-induced conversion of nitrate to N_2. In the presence of NH_3 as an electron donor (*i.e.*, using the same concept as that discussed in Section 2.2.1, the photo-SCR deNO_x), ammonia oxidation and denitrification simultaneously occurred over TiO_2 and Pt black, respectively, in the absence of a bias voltage under UV light irradiation (1 mM NH_3, 100 mM KNO_3) (Fig. 15a).[214] When a mixture of pig urine/wash water (1/4) containing NH_4^+, NO_3^-, and NO_2^- was tested under aerobic conditions, the following concentration decreases were observed after 24 h: NH_4^+ (2580 → 166 ppm), NO_3^- (18.6 → 17.0 ppm), and NO_2^- (4.84 → 3.17 ppm). The imbalance in the removal of NO_x^- and NH_4^+ was ascribed to the competitive reduction of oxygen to H_2O. Similarly, in a biophotochemical cell, H_2O or biorefractory organics were oxidized at the photoanode, while denitrification proceeded at the biocathode.[215,216] The biocathode was prepared using activated sludge as an inoculum and was separated from the TiO_2 photoanode by a cation exchange membrane. As seen in Fig. 15b, the concentration of nitrate continuously decreased under illumination, whereas the abiotic cathode did not show any activity. Indeed, NO_2^- and N_2O were formed as intermediates, but the concentration of these intermediates and NO_3^- decreased to zero after 30 h (Fig. 15c). NH_4^+ ions were always present at levels below the detection limit, which indicated that nitrate was selectively converted to N_2. The faradaic efficiency of the cathode was

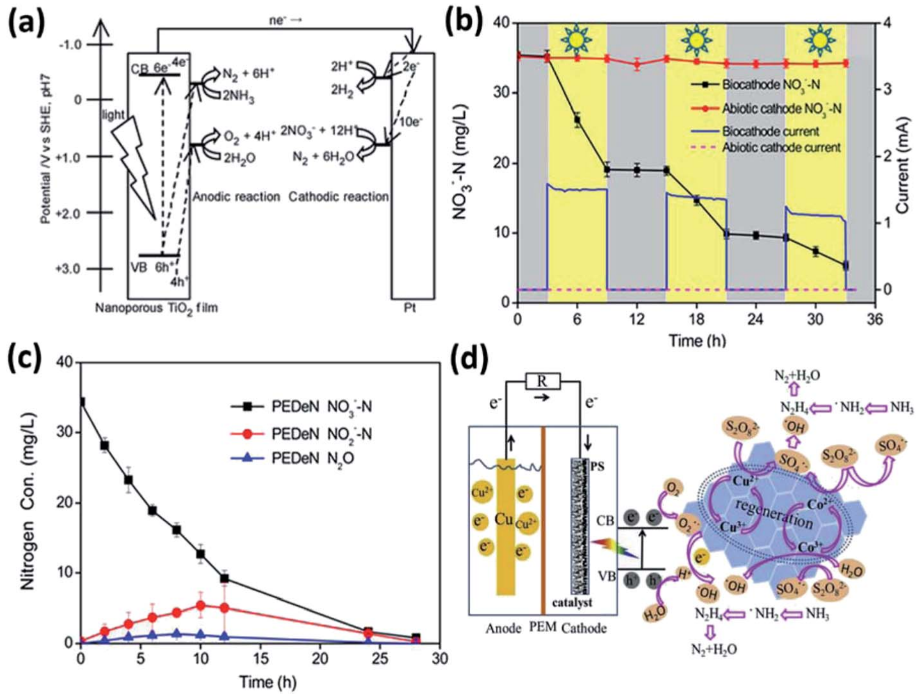

Fig. 15 (a) Photoelectrochemical denitrification of NO_3^- to N_2 over a TiO_2 photoanode connected to a Pt cathode in the presence of NH_3 and H_2O as electron donors under Ar. Reprinted with permission from ref. 214. Copyright© 2009, Royal Society of Chemistry. (b) Decrease of nitrate level under a photo-generated current during on–off intermittent illumination and (c) change of nitrogen oxide levels with time. Reprinted with permission from ref. 215. Copyright© 2017, American Chemical Society. (d) Proposed mechanism for the oxidation of NH_3 over a CuO/Co_3O_4 photocathode in the presence of peroxydisulfate. Reprinted with permission from ref. 219. Copyright© 2020, Elsevier.

estimated as 97%, and a small number of electrons was assumed to be consumed by microbial growth.

The photoelectrochemical oxidation of ammonia to N_2 can be accomplished using the anodic or cathodic reaction to control photogenerated holes or radical species (hydroxyl or sulfate radicals) activated by electrons, respectively.[217–220] In the employed system (CE = Pt wire, RE = Ag/AgCl, and WE = TiO_2 photoanode in 10 M NH_3 + 0.1 M KNO_3 at pH 14.1), the $H_2 : N_2$ molar ratio equaled 3.08 under short-circuit conditions after 2 h irradiation.[188] The holes in TiO_2 oxidized NH_3 to N_2, and the electrons transferred to Pt reduced water to H_2. The $OH^\bullet$ and $SO_4^{\bullet-}$ species generated by the activation of peroxydisulfate ($S_2O_8^{2-} + e^- \rightarrow SO_4^{\bullet-} + SO_4^{2-}$ and $SO_4^{\bullet-} + H_2O \rightarrow H^+ + OH^\bullet + SO_4^{2-}$) at the CuO/Co_3O_4 photocathode oxidized NH_3 to N_2 (Fig. 15d).[219] The removal of 96.1% NH_3 (100 ppm) was achieved under visible light irradiation, and the reactive sites were identified as Co and Cu species.

5. Summary and outlook

There are various methods of decreasing the levels of reactive nitrogen compounds, which can include systematic crop rotation, optimization of the timing and amount of fertilizer input, the breeding or development of genetically engineered varieties of crops for increased nitrogen utilization efficiency, direct upcycling of used nitrogen to microbial protein, and the development of artificial denitrification/ammonia oxidation processes powered by renewable energy. Among them, the solar-powered photocatalytic and photoelectrochemical approaches are promising and future-oriented ways to treat aqueous and airborne NO_x, N_2O, and NH_3 because of their economically feasible and environmentally benign nature. However, the low efficiency and selectivity to N_2 and the scale-up problems are still a bottleneck for practical applications. Basically, the efficiency of artificial solar-powered denitrification/ammonia oxidation can be determined by (i) the absorbance of photocatalysts, (ii) the electronic structure of semiconducting materials, (iii) the recombination of charge carriers (*i.e.*, the lifetime of photogenerated electrons and holes), (iv) the control of surface properties to suppress undesired reactions such as ammonification and the re-oxidation of intermediates and products, and (v) the surroundings (*e.g.*, the presence/absence of oxygen, different types of electron donors, pH, humidity, *etc.*). Due to the different reaction pathways, the development of new photocatalysts and the systematic design of reactors have to be different depending on the treatment of aqueous and gas phase NO_x, N_2O, and NH_3. In an aqueous system, the bimetallic nanoparticles loaded on TiO_2 (*e.g.*, Pd–Cu and Pt–Cu) showed a high performance of NO_3^- conversion selective to N_2, which gives a hint that the separation of the catalytic sites, the reduction of NO_3^- to NO_2^- and the further reduction of NO_2^- to N_2, is important to increase the selectivity. Precise control of the N : H ratio at surface active sites of catalysts including Lewis acid sites and defect sites is particularly required to suppress ammonification and thus selectively convert NO_2^- to harmless N_2. The reason why it is hard to reach a high conversion efficiency of NO_3^- or NO_2^- as well as a high selectivity to N_2 is due to the competitive charge transfer to H^+, O_2, and H_2O and the re-oxidation of intermediates and by-products. In the case of the photocatalytic treatment of airborne NO_x and N_2O to N_2, it has been thoroughly investigated during the last three decades, offering the advantages of using water instead of the explosive H_2 and toxic NH_3, operation at standard temperature and pressure, a net zero carbon emission in the case of operation under natural sunlight, and the availability of cheap and environmentally benign materials. Although various strategies such as structure and morphology control, co-catalyst loading, heteroatom doping, and hybridization with different types of materials have been developed to overcome the bottleneck of the conversion of NO_x and N_2O to N_2, the problems of insufficiently selective charge transfer, low solar light absorption, poor catalytic activity, need for noble metals as co-catalysts, and the lack of long-term durability need to be addressed to minimize the environmental impact of airborne NO_x and N_2O. In order to increase the possibility of commercialization, the addition of sacrificial hole scavengers should be necessary, where organic pollutants, particularly persistent organic pollutants (POPs), and ammonia (or carbon monoxide) are good candidates for wastewater and polluted air treatment, respectively, to compensate the operation cost.

Although ammonia is a very important feedstock, its high toxicity, corrosivity, and noxious odor make it a pollutant from the perspective of the environmental management of the nitrogen cycle. Given the large annual production of ammonia *via* the Haber–Bosch process and the low nitrogen use efficiency of ammonia-based fertilizers, ammonia should be effectively removed from air and water on a comparable scale. Recently, considering ammonia as a hydrogen carrier, the development of highly active catalysts for the decomposition of ammonia to H_2 and N_2 under mild conditions is highly desired. Although the conventional photocatalytic processes have focused on ammonia abatement, directing the production of nitrate instead of N_2, with a future-oriented point of view, the photocatalytic recovery of H_2 from concentrated ammonia solution seems quite promising for fuel cell applications. The oxidation of adsorbed NH_3 occurring *via* photogenerated holes does not involve the formation of NO_x, but the $H_2 : N_2$ molar ratio becomes close to the theoretical value of $3 : 1$ through the decomposition of NH_3 to N_2 and H_2, which is driven at standard temperature and pressure under illumination.

A photoelectrochemical cell can selectively control the reduction and oxidation reaction of nitrogen-containing species, in which the photogenerated electron–hole pairs are easily separated and consequently participate in the denitrification and anammox upon applying extra bias. To date, very few studies have been reported, in particular targeting the removal of toxic nitrite and ammonia from wastewater; however, the application should be more suitable for anammox in order to secure H_2 from concentrated ammonia. Contrary to photocatalysis, it does not need to separate N_2 and H_2 because the oxidation and the reduction are proceeded in the anode and cathode, respectively, which is comparted by a membrane. Indeed, the addition of an electrolyte is unnecessary in that the pH of concentrated ammonia solution (>12) is conductive enough to transport ions in the electrolyte. The in-depth investigation and successful development of photoelectrochemical ammonia oxidation systems will enable a counterpart of (photo)electrocatalytic nitrogen fixation, in other words the combination of the production and the utilization of ammonia as a hydrogen carrier.

It is time to take this issue seriously and think about it, and photocatalysis is the greenest way to restore the nitrogen cycle with a future-oriented technology. In order to go one step further to commercialization, the following can be considered: (i) the development of new materials to overcome the intrinsic problems of photocatalysts, (ii) the control of composition, morphology, and size of catalysts (*e.g.*, high entropy alloy, single atom catalyst, *etc.*), (iii) the systematic modification of photocatalysts including hybridization such as ternary and quaternary composites, co-doping, anchoring homogeneous sensitizers or promoters, selective surface passivation, *etc.*, (iv) the separation of catalytic sites by the control of the boundary between the catalysts and supporter or by a Janus structure, (v) the precise control of the micro-environment on the catalysts or electrodes, (vi) the finding of suitable POPs and greenhouse gases that cannot be removed by conventional treatment or typical AOPs, (vii) the design of a photo-reactor and its scale-up, (viii) the combination with other processes such as the pretreatment or final treatment through biological processes, and (ix) *in situ* analysis (*e.g.*, time-resolved surface enhanced infrared absorption/Raman spectroscopy) to unveil the real-time charge transfer and the formation of intermediates for the optimization of desired reactions.

Author contributions

Cheolwoo Park: investigation, visualization, writing – original draft. Hyelim Kwak: investigation, visualization, writing – original draft. Gun-hee Moon: conceptualization, supervision, writing – original draft. Wooyul Kim: conceptualization, supervision, writing – review & editing.

Conflicts of interest

There are no conflicts to declare.

Acknowledgements

This research was financially supported by the Basic Science Research Program (NRF-2019R1C1C1006833) funded by the Korea government (MSIT) through the National Research Foundation of Korea (NRF), the Ecological Imitation-Based Environmental Pollution Management Technology Development Project funded by the Korea government (MOE) through KEITI (No. 2019002790008), the National Research Foundation of Korea (NRF) funded by the Ministry of Science and ICT (NRF-2020M3H4A3106354), and the KIST internal project (3E311191) funded by the Korea Institute of Science and Technology (KIST).

Notes and references

1 A. Bernhard, *Nat. Educ. Knowl.*, 2010, **2**, 1–8.
2 D. E. Canfield, A. N. Glazer and P. G. Falkowski, *Science*, 2010, **330**, 192–196.
3 J. N. Galloway, A. M. Leach, A. Bleeker and J. W. Erisman, *Philos. Trans. R. Soc., B*, 2013, **368**, 20130120.
4 M. A. Sutton, C. M. Howard, T. K. Adhya, E. Baker, J. Baron, A. Basir, W. Brownlie, C. Cordovil, W. de Vries, V. Eory, R. Green, H. Harmens, K. W. Hicks, R. Jeffery, D. Kanter, L. Lassaletta, A. Leip, C. Masso, T. H. Misselbrook, E. Nemitz, S. P. Nissanka, O. Oenema, S. Patra, M. Pradhan, J. Ometto, R. Purvaja, N. Raghuram, R. Ramesh, N. Read, D. S. Reay, E. Rowe, A. SanzCobena, S. Sharma, K. R. Sharp, U. Skiba, J. U. Smith, I. van der Beck, M. Vieno, and H. J. M. van Grinsven, *Nitrogen - Grasping the Challenge. A Manifesto for Science-In-Action through the International Nitrogen Management System*. Summary Report, Ecology & Hydrology, Edinburgh, UK, 2019.
5 Food and Agriculture Organization, *FAO Statistical Databases*, 2006, Rome, available at http://faostat.fao.org/default.aspx.
6 International Energy Agency, *IEA Statistical Databases*, 2015, Paris, available at http://iea.org/data-and-statistics.
7 *Revised 1996 IPCC Guidelines for National Greenhouse Gas Inventories*, ed. J. T. Houghton, L. G. Meria Filho, K. Lim, I. Trennton, I. Mamaty, Y. Bonduki, D. J. Griggs and B. A. Callander, IPCC, OECD, IEA, 1996.
8 D. Laffoley and J. M. Baxter, *Ocean Deoxygenation: Everyone's Problem*, IUCN, Global Marine and Polar Programme, 2019.
9 N. Gruber and J. N. Galloway, *Nature*, 2008, **451**, 293–296.
10 S. Matassa, D. J. Batstone, T. Hülsen, J. Schnoor and W. Verstraete, *Environ. Sci. Technol.*, 2015, **49**, 5247–5254.
11 S. P. Seitzinger, C. Kroeze, A. F. Bouwman, N. Caraco, F. Dentener and R. V. Styles, *Estuaries*, 2002, **25**, 640–655.
12 M. B. Peoples, J. Brockwell, D. F. Herridge, I. J. Rochester, B. J. R. Alves, S. Urquiaga, R. M. Boddey, F. D. Dakora, S. Bhattarai, S. L. Maskey, C. Sampet, B. Rerkasem, D. F. Khan, H. Hauggaard-Nielsen and E. S. Jensen, *Symbiosis*, 2009, **48**, 1–17.
13 Y. Lan, J. Chen, H. Zhang, W.-X. Zhang and J. Yang, *J. Mater. Chem. A*, 2020, **8**, 15853–15863.
14 W. Hong, L. Su, J. Wang, M. Jiang, Y. Ma and J. Yang, *Chem. Commun.*, 2020, **56**, 14685–14688.
15 F. Ni, Y. Ma, J. Chen, W. Luo and J. Yanga, *Chin. Chem. Lett.*, 2021, **32**, 2073–2078.
16 L. Su, D. Han, G. Zhu, H. Xu, W. Luo, L. Wang, W. Jiang, A. Dong and J. Yang, *Nano Lett.*, 2019, **19**, 5423–5430.
17 H. Xu, J. Wu, W. Luo, Q. Li, W. Zhang and J. Yang, *Small*, 2020, **16**, 2001775.
18 D. R. Keeney, R. L. Chen and D. A. Graetz, *Nature*, 1971, **233**, 66–67.
19 A. Kapoor and T. Viraraghavan, *J. Environ. Eng.*, 1997, **123**, 371–380.
20 H. O. N. Tugaoen, S. Garcia-Segura, K. Hristovski and P. Westerhoff, *Sci. Total Environ.*, 2017, **599–600**, 1524–1551.
21 Z. Geng, Z. Chen, Z. Li, X. Qi, X. Yang, W. Fan, Y. Guo, L. Zhang and M. Huo, *Dalton Trans.*, 2018, **47**, 11104–11112.
22 H. Xu, Y. Li, M. Ding, W. Chen, K. Wang and C. Lu, *ACS Sustainable Chem. Eng.*, 2018, **6**, 7042–7051.
23 S. Roy, *J. Phys. Chem. C*, 2020, **124**, 28345–28358.
24 H. Zhang, Z. Liu, Y. Li, C. Zhang, Y. Wang, W. Zhang, L. Wang, L. Niu, P. Wang and C. Wang, *Appl. Surf. Sci.*, 2020, **503**, 144092.
25 J. E. Silveira, A. R. Ribeiro, J. Carbajo, G. Pliego, J. A. Zazo and J. A. Casas, *Water Res.*, 2021, **200**, 117250.
26 L. Wang, W. Fu, Y. Zhuge, J. Wang, F. Yao, W. Zhong and X. Ge, *Chemosphere*, 2021, **278**, 130298.
27 T. Caswell, M. W. Dlamini, P. J. Miedziak, S. Pattisson, P. R. Davies, S. H. Taylor and G. J. Hutchings, *Catal. Sci. Technol.*, 2020, **10**, 2082–2091.
28 H. Kominami, K. Kitsui, Y. Ishiyama and K. Hashimoto, *RSC Adv.*, 2014, **4**, 51576–51579.
29 H. Gekko, K. Hashimoto and H. Kominami, *Phys. Chem. Chem. Phys.*, 2012, **14**, 7965–7970.
30 W. L. Silver, D. J. Herman and M. K. Firestone, *Ecology*, 2001, **82**, 2410–2416.
31 E. M. Sander, B. Virdis and S. Freguia, *RSC Adv.*, 2015, **5**, 86572–86577.
32 H. Hirakawa, M. Hashimoto, Y. Shiraishi and T. Hirai, *ACS Catal.*, 2017, **7**, 3713–3720.
33 H. Kominami, A. Furusho, S.-y. Murakami, H. Inoue, Y. Kera and B. Ohtani, *Catal. Lett.*, 2001, **76**, 31–34.
34 K. Akihiko, D. Kazunari, M. Ken-ichi and O. Takaharu, *Chem. Lett.*, 1987, **16**, 1019–1022.
35 M. Duca and M. T. M. Koper, *Energy Environ. Sci.*, 2012, **5**, 9726–9742.
36 Z. Hou, J. Chu, C. Liu, J. Wang, A. Li, T. Lin and C. P. François-Xavier, *Chem. Eng. J.*, 2021, **415**, 2082–2091.
37 S. Lee, S. Kim, C. Park, W. Kim, S. Ryu and W. Choi, *Energy Environ. Sci.*, 2021, DOI: 10.1039/D1EE01342D.
38 P. Li, Z. Jin, Z. Fanga and G. Yu, *Energy Environ. Sci.*, 2021, **14**, 3522–3531.
39 M. Shand and J. A. Anderson, *Catal. Sci. Technol.*, 2013, **3**, 879–899.
40 H.-i. Kim, K. Kim, S. Park, W. Kim, S. Kim and J. Kim, *Sep. Purif. Technol.*, 2019, **209**, 580–587.
41 L. Lei, W. Wang, C. Wang, H. Fan, A. K. Yadav, N. Hu, Q. Zhong and P. Müller-Buschbaum, *J. Mater. Chem. A*, 2020, **8**, 23812–23819.
42 Q. Liu, S. Wang, Q. Ren, T. Li, G. Tu, S. Zhong, Y. Zhao and S. Bai, *J. Mater. Chem. A*, 2021, **9**, 1552–1562.
43 X. Li, H. Jiang, C. Ma, Z. Zhu, X. Song, X. Li, H. Wang, P. Huo and X. Chen, *J. Mater. Chem. A*, 2020, **8**, 18707–18714.
44 S. Lee, S. Kim, C. Park, G.-h. Moon, H.-J. Son, J.-O. Baeg, W. Kim and W. Choi, *ACS Sustainable Chem. Eng.*, 2020, **8**, 3709–3717.

45 H. Lee, S. Jee, R. Kim, H.-T. Bui, B. Kim, J.-K. Kim, K. Park, W. Choi, W. Kim and K. Choi, *Energy Environ. Sci.*, 2020, **13**, 519–526.
46 E.-T. Yun, H.-Y. Yoo, W. Kim, H.-E. Kim, G. Kang, H. Lee, S. Lee, T. Park, C. Lee, J.-H. Kim and J. Lee, *Appl. Catal., B*, 2017, **203**, 475–484.
47 Y. Zhang, W. Hu, D. Wang, B. J. Reinhart and J. Huang, *J. Mater. Chem. A*, 2021, **9**, 6180–6187.
48 S. Weon, E. Choi, H. Kim, J. Kim, H.-J. Park, S.-m. Kim, W. Kim and W. Choi, *Environ. Sci. Technol.*, 2018, **52**, 9330–9340.
49 Q. Guo, F. Liang, Z. Sun, Y. Wang, X.-B. Li, S.-G. Xia, Z. C. Zhang, L. Huang and L.-Z. Wu, *J. Mater. Chem. A*, 2020, **8**, 22601–22606.
50 J. Sá, C. A. Agüera, S. Gross and J. A. Anderson, *Appl. Catal., B*, 2009, **85**, 192–200.
51 J. A. Anderson, *Catal. Today*, 2011, **175**, 316–321.
52 W. Gao, R. Jin, J. Chen, X. Guan, H. Zeng, F. Zhang and N. Guan, *Catal. Today*, 2004, **90**, 331–336.
53 S. Rengaraj and X. Z. Li, Enhanced photocatalytic reduction reaction over Bi3+-TiO2 nanoparticles in presence of formic acid as a hole scavenger, *Chemosphere*, 2007, **66**, 930–9383.
54 D. D. B. Luiz, S. L. F. Andersen, C. Berger, H. J. José and R. D. F. P. M. Moreira, *J. Photochem. Photobiol. A*, 2012, **246**, 36–44.
55 J. R. Pan, C. Huang, W. Hsieh and B. Wu, *Sep. Purif. Technol.*, 2012, **84**, 52–55.
56 K. Kobwittaya and S. Sirivithayapakorn, *APCBEE Proc.*, 2014, **10**, 321–325.
57 S.-E. Bae, K. L. Stewart and A. A. Gewirth, *J. Am. Chem. Soc.*, 2007, **129**, 10171–10180.
58 I. Sanjuán, L. García-Cruz, J. Solla-Gullón, E. Expósito and V. Montiel, *Electrochim. Acta*, 2020, **340**, 135914.
59 S. Hamid, M. A. Kumar, J.-I. Han, H. Kim and W. Lee, *Green Chem.*, 2017, **19**, 853–866.
60 H. Shin, S. Jung, S. Bae, W. Lee and H. Kim, *Environ. Sci. Technol.*, 2014, **48**, 12768–12774.
61 T. Gu, W. Teng, N. Bai, Z. Chen, J. Fan, W.-x. Zhang and D. Zhao, *J. Mater. Chem. A*, 2020, **8**, 9545–9553.
62 S. Jung, S. Bae and W. Lee, *Environ. Sci. Technol.*, 2014, **48**, 9651–9658.
63 A. J. Calandra, C. Tamayo, J. Herrera and A. J. Arvía, *Electrochim. Acta*, 1972, **17**, 2035–2053.
64 L. Li, Z. Xu, F. Liu, Y. Shao, J. Wang, H. Wan and S. Zheng, *J. Photochem. Photobiol., A*, 2010, **212**, 113–121.
65 H. Kominami, T. Nakaseko, Y. Shimada, A. Furusho, H. Inoue, S.-y. Murakami, Y. Kera and B. Ohtani, *Chem. Commun.*, 2005, 2933–2935.
66 O. S. G. P. Soares, M. F. R. Pereira, J. J. M. Órfão, J. L. Faria and C. G. Silva, *Chem. Eng. J.*, 2014, **251**, 123–130.
67 Z. Hou, F. Chen, J. Wang, C. P. François-Xavier and T. Wintgens, *Appl. Catal., B*, 2018, **232**, 124–134.
68 J. A. Zazo, P. García-Muñoz, G. Pliego, J. E. Silveira, P. Jaffe and J. A. Casas, *Appl. Catal., B*, 2020, **273**, 118930.
69 H. Kato and A. Kudo, *Phys. Chem. Chem. Phys.*, 2002, **4**, 2833–2838.
70 L. Mohapatra and K. Parida, *J. Mater. Chem. A*, 2016, **4**, 10744–10766.
71 N. Dewangan, W. M. Hui, S. Jayaprakash, A.-R. Bawah, A. J. Poerjoto, T. Jie, A. Jangam, K. Hidajat, S. Kawi, *Catal. Today*, **356**, 490–513.
72 S. Zhang, Y. Zhao, R. Shi, C. Zhou, G. I. N. Waterhouse, L.-Z. Wu, C.-H. Tung and T. Zhang, *Adv. Energy Mater.*, 2020, **10**, 1901973.
73 D. P. Sahoo, K. K. Das, S. Patnaik and K. Parida, *Inorg. Chem. Front.*, 2020, **7**, 3695–3717.
74 Y. Zhao, G. Chen, T. Bian, C. Zhou, G. I. N. Waterhouse, L.-Z. Wu, C.-H. Tung, L. J. Smith, D. O'Hare and T. Zhang, *Adv. Mater.*, 2015, **27**, 7824–7831.
75 M. Adachi and A. Kudo, *Chem. Lett.*, 2012, **41**, 1007–1008.
76 X. Li, S. Wang, H. An, G. Dong, J. Feng, T. Wei, Y. Ren and J. Ma, *Appl. Surf. Sci.*, 2021, **539**, 148257.
77 M. Yue, R. Wang, B. Ma, R. Cong, W. Gao and T. Yang, *Catal. Sci. Technol.*, 2016, **6**, 8300–8308.
78 R. Wang, M. Yue, R. Cong, W. Gao and T. Yang, *J. Alloys Compd.*, 2015, **651**, 731–736.
79 B. Wang, B. An, Z. Su, L. Li and Y. Liu, *Chemosphere*, 2021, **269**, 128754.
80 G. Liu, S. You, M. Ma, H. Huang and N. Ren, *Environ. Sci. Technol.*, 2016, **50**, 11218–11225.
81 H.-T. Ren, S.-Y. Jia, J.-J. Zou, S.-H. Wu and X. Han, *Appl. Catal., B*, 2015, **176–177**, 53–61.
82 Y. Li and F. Wasgestian, *J. Photochem. Photobiol., A*, 1998, **112**, 255–259.
83 J. A. Anderson, *Catal. Today*, 2012, **181**, 171–176.
84 B. Bems, F. C. Jentoft and R. Schlögl, *Appl. Catal., B*, 1999, **20**, 155–163.
85 F. Zhang, Y. Pi, J. Cui, Y. Yang, X. Zhang and N. Guan, *J. Phys. Chem. C*, 2007, **111**, 3756–3761.
86 J. M. A. Freire, M. A. F. Matos, D. S. Abreu, H. Becker, I. C. N. Diógenes, A. Valentini and E. Longhinotti, *J. Environ. Chem. Eng.*, 2020, **8**, 103844.
87 A. Oita, A. Malik, K. Kanemoto, A. Geschke, S. Nishijima and M. Lenzen, *Nat. Geosci.*, 2016, **9**, 111–115.
88 D. S. Reay, E. A. Davidson, K. A. Smith, P. Smith, J. M. Melillo, F. Dentener and P. J. Crutzen, *Nat. Clim. Change*, 2012, **2**, 410–416.
89 G. Busca, L. Lietti, G. Ramis and F. Berti, *Appl. Catal., B*, 1998, **18**, 1–36.
90 L. Yang, A. Hakki, F. Wang and D. E. Macphee, *Appl. Catal., B*, 2018, **222**, 200–208.
91 Z. Gu, B. Zhang, Y. Asakura, S. Tsukuda, H. Kato, M. Kakihana and S. Yin, *Appl. Surf. Sci.*, 2020, **521**, 146213.
92 V. Khanal, N. O. Balayeva, C. Günnemann, Z. Mamiyev, R. Dillert, D. W. Bahnemann and V. R. Subramanian, *Appl. Catal., B*, 2021, **291**, 119974.
93 G. Liu, H. Xia, W. Zhang, L. Song, Q. Chen and Y. Niu, *J. Hazard. Mater.*, 2021, **418**, 126337.
94 J. V. C. d. Carmo, C. L. Lima, G. Mota, A. M. S. Santos, L. N. Costa, A. Ghosh, B. C. Viana, M. Silva, J. M. Soares, S. Tehuacanero-Cuapa, R. Lang, A. C. Oliveira, E. Rodríguez-Castellón and E. Rodríguez-Aguado, *Materials*, 2021, **14**, 2181.

95 W. Kim, T. Tachikawa, G.-h. Moon, T. Majima and W. Choi, *Angew. Chem., Int. Ed.*, 2014, **53**, 14036–14041.
96 Q. Wu and R. van de Krol, *J. Am. Chem. Soc.*, 2012, **134**, 9369–9375.
97 Q. Wu, Q. Zheng and R. van de Krol, *J. Phys. Chem. C*, 2012, **116**, 7219–7226.
98 G. Dong, D. L. Jacobs, L. Zang and C. Wang, *Appl. Catal., B*, 2017, **218**, 515–524.
99 M. Anpo, Y. Shioya, H. Yamashita, E. Giamello, C. Morterra, M. Che, H. H. Patterson, S. Webber and S. Ouellette, *J. Phys. Chem.*, 1994, **98**, 5744–5750.
100 M. Matsuoka, E. Matsuda, K. Tsuji, H. Yamashita and M. Anpo, *J. Mol. Catal. A: Chem.*, 1996, **107**, 399–403.
101 W.-S. Ju, M. Matsuoka and M. Anpo, *Catal. Lett.*, 2001, **71**, 91–93.
102 M. Anpo, S. G. Zhang, H. Mishima, M. Matsuoka and H. Yamashita, *Catal. Today*, 1997, **39**, 159–168.
103 Y. Hu, G. Martra, J. Zhang, S. Higashimoto, S. Coluccia and M. Anpo, *J. Phys. Chem. B*, 2006, **110**, 1680–1685.
104 M. Matsuoka and M. Anpo, in *Catalysis by Unique Metal Ion Structures in Solid Matrices*, ed. G. Centi, B. Wichterlová and A. T. Bell, Springer, Dordrecht, 2001, ch. Photocatalysis of Cations Incorporated within Zeolites, vol. 13, pp. 249–262.
105 M. Anpo, M. Matsuoka, K. Hanou, H. Mishima, H. Yamashita and H. H. Patterson, *Coord. Chem. Rev.*, 1998, **171**, 175–184.
106 M. Anpo and J. M. Thomas, *Chem. Commun.*, 2006, 3273–3278.
107 N. W. Cant and J. R. Cole, *J. Catal.*, 1992, **134**, 317–330.
108 T. Shishido, K. Teramura and T. Tanaka, *Catal. Sci. Technol.*, 2011, **1**, 541–551.
109 A. Yamamoto, K. Teramura and T. Tanaka, *Chem. Rec.*, 2016, **16**, 2268–2277.
110 K. Teramura, T. Tanaka and T. Funabiki, *Langmuir*, 2003, **19**, 1209–1214.
111 K. Teramura, T. Tanaka, S. Yamazoe, K. Arakaki and T. Funabiki, *Appl. Catal., B*, 2004, **53**, 29–36.
112 S. Yamazoe, T. Okumura, K. Teramura and T. Tanaka, *Catal. Today*, 2006, **111**, 266–270.
113 Y. Ji and Y. Luo, *J. Phys. Chem. C*, 2014, **118**, 6359–6364.
114 S. Yamazoe, Y. Masutani, T. Shishido and T. Tanaka, *Res. Chem. Intermed.*, 2008, **34**, 487–494.
115 S. Yamazoe, Y. Masutani, K. Teramura, Y. Hitomi, T. Shishido and T. Tanaka, *Appl. Catal., B*, 2008, **83**, 123–130.
116 R. Jin, Z. Wu, Y. Liu, B. Jiang and H. Wang, *J. Hazard. Mater.*, 2009, **161**, 42–48.
117 Y.-C. Chou and Y. Ku, *Chem. Eng. J.*, 2013, **225**, 734–743.
118 S. Yamazoe, K. Teramura, Y. Hitomi, T. Shishido and T. Tanaka, *J. Phys. Chem. C*, 2007, **111**, 14189–14197.
119 G. Zhang, G. Kim and W. Choi, *Energy Environ. Sci.*, 2014, **7**, 954–966.
120 A. Yamamoto, Y. Mizuno, K. Teramura, S. Hosokawa, T. Shishido and T. Tanaka, *Catal. Sci. Technol.*, 2015, **5**, 556–561.
121 A. Yamamoto, K. Teramura, S. Hosokawa, T. Shishido and T. Tanaka, *ChemCatChem*, 2015, **7**, 1818–1825.
122 X. Li, X. Yan, S. Zuo, X. Lu, S. Luo, Z. Li, C. Yao and C. Ni, *Chem. Eng. J.*, 2017, **320**, 211–221.
123 H. Zhang, X. Li, Y. Hui, L. Yu, Q. Xia, S. Luo and C. Yao, *J. Mater. Sci.: Mater. Electron.*, 2017, **28**, 9371–9377.
124 X. Li, H. Shi, W. Zhu, S. Zuo, X. Lu, S. Luo, Z. Li, C. Yao and Y. Chen, *Appl. Catal., B*, 2018, **231**, 92–100.
125 K. Wei, X. Yan, S. Zuo, W. Zhu, F. Wu, X. Li, C. Yao and X. Liu, *Clays Clay Miner.*, 2019, **67**, 348–356.
126 Z. Zhang, H. Lü, X. Li, X. Li, S. Ran, Z. Chen, Y. Yang, X. Wu and L. Li, *ACS Sustainable Chem. Eng.*, 2019, **7**, 10299–10309.
127 X. Li, H. Shi, X. Yan, S. Zuo, Y. Zhang, T. Wang, S. Luo, C. Yao and C. Ni, *ACS Sustainable Chem. Eng.*, 2018, **6**, 10616–10627.
128 X. Li, H. Shi, T. Wang, Y. Zhang, X. Lu, S. Zuo, Z. Li and C. Yao, *J. Taiwan Inst. Chem. Eng.*, 2018, **89**, 119–128.
129 X. Li, X. Yan, X. Lu, S. Zuo, Z. Li, C. Yao and C. Ni, *J. Catal.*, 2018, **357**, 59–68.
130 X. Li, H. Shi, X. Yan, S. Zuo, Y. Zhang, Q. Chen, C. Yao and C. Ni, *J. Catal.*, 2019, **369**, 190–200.
131 X. Li, Z. Wang, H. Shi, D. Dai, S. Zuo, C. Yao and C. Ni, *J. Hazard. Mater.*, 2020, **386**, 121977.
132 X. Li, H. Zhang, H. Lü, S. Zuo, Y. Zhang and C. Yao, *Environ. Sci. Pollut. Res.*, 2019, **26**, 12842–12850.
133 X. Li, Z. Wang, X. Chu, B. Gao, S. Zuo, W. Liu and C. Yao, *Appl. Clay Sci.*, 2020, **199**, 105871.
134 H. I. Hamoud, M. Lafjah, F. Douma, O. I. Lebedev, F. Djafri, V. Valchev, M. Daturi and M. El-Roz, *Sol. Energy*, 2019, **189**, 244–253.
135 N. Bowering, G. S. Walker and P. G. Harrison, *Appl. Catal., B*, 2006, **62**, 208–216.
136 N. Bowering, D. Croston, P. G. Harrison and G. S. Walker, *Int. J. Photoenergy*, 2007, **2007**, 090752.
137 A. A. Lisachenko, R. V. Mikhailov, L. L. Basov, B. N. Shelimov and M. Che, *J. Phys. Chem. C*, 2007, **111**, 14440–14447.
138 C. H. Ao, S. C. Lee, C. L. Mak and L. Y. Chan, *Appl. Catal., B*, 2003, **42**, 119–129.
139 S. Poulston, M. V. Twigg and A. P. Walker, *Appl. Catal., B*, 2009, **89**, 335–341.
140 Y.-T. Wu, Y.-H. Yu, V.-H. Nguyen and J. C. S. Wu, *Res. Chem. Intermed.*, 2015, **41**, 2153–2164.
141 Y.-H. Yu, I.-H. Su and J. C. S. Wu, *Environ. Technol.*, 2010, **31**, 1449–1458.
142 J. Lasek, Y.-H. Yu and J. C. S. Wu, *Environ. Technol.*, 2012, **33**, 2133–2141.
143 Y.-H. Yu, Y.-T. Pan, Y.-T. Wu, J. Lasek and J. C. S. Wu, *Catal. Today*, 2011, **174**, 141–147.
144 I. H. Su and J. C. S. Wu, *Catal. Commun.*, 2009, **10**, 1534–1537.
145 J. C.-C. Yu, V.-H. Nguyen, J. Lasek, S.-W. Chiang, D. X. Li and J. C. S. Wu, *Appl. Catal., A*, 2016, **523**, 294–303.
146 J. C.-C. Yu, V.-H. Nguyen, J. Lasek and J. C. S. Wu, *Appl. Catal., B*, 2017, **219**, 391–400.
147 J. C.-C. Yu, V.-H. Nguyen, J. Lasek, D. X. Li and J. C. S. Wu, *Catal. Commun.*, 2016, **84**, 40–43.

148 J. Miyawaki, T. Shimohara, N. Shirahama, A. Yasutake, M. Yoshikawa, I. Mochida and S.-H. Yoon, *Appl. Catal., B*, 2011, **110**, 273–278.
149 G. Halasi, T. Bánsági and F. Solymosi, *J. Catal.*, 2015, **325**, 60–67.
150 L. Liao, S. Heylen, S. P. Sree, B. Vallaey, M. Keulemans, S. Lenaerts, M. B. J. Roeffaers and J. A. Martens, *Appl. Catal., B*, 2017, **202**, 381–387.
151 G. Blyholder and K. Tanaka, *J. Phys. Chem.*, 1971, **75**, 1037–1043.
152 J. Cunningham, J. J. Kelly and A. L. Penny, *J. Phys. Chem.*, 1971, **75**, 617–625.
153 N. B. Wong, Y. B. Taarit and J. H. Lunsford, *J. Chem. Phys.*, 1974, **60**, 2148–2151.
154 M. Anpo, N. Aikawa and Y. Kubokawa, *J. Chem. Soc., Chem. Commun.*, 1984, 644–645.
155 M. Anpo, N. Aikawa, Y. Kubokawa, M. Che, C. Louis and E. Giamello, *J. Phys. Chem.*, 1985, **89**, 5689–5694.
156 A. Kudo and T. Sakata, *Chem. Lett.*, 1992, **21**, 2381–2384.
157 A. Kudo and H. Nagayoshi, *Catal. Lett.*, 1998, **52**, 109–111.
158 T. Sano, N. Negishi, D. Mas and K. Takeuchi, *J. Catal.*, 2000, **194**, 71–79.
159 M. Matsuoka, W.-S. Ju, K. Takahashi, H. Yamashita and M. Anpo, *J. Phys. Chem. B*, 2000, **104**, 4911–4915.
160 K. Ebitani, M. Morokuma, J.-H. Kim and A. Morikawa, *J. Catal.*, 1993, **141**, 725–728.
161 K. Ebitani, M. Morokuma, J.-H. Kim and A. Morikawa, *J. Chem. Soc., Faraday Trans.*, 1994, **90**, 377–381.
162 K. Ebitani, M. Morokuma and A. Morikawa, in *Stud. Surf. Sci. Catal.*, ed. J. Weitkamp, H. G. Karge, H. Pfeifer and W. Hölderich, Elsevier, 1994, vol. 84, pp. 1501–1506.
163 W.-S. Ju, M. Matsuoka, K. Iino, H. Yamashita and M. Anpo, *J. Phys. Chem. B*, 2004, **108**, 2128–2133.
164 W.-S. Ju, M. Matsuoka, H. Yamashita and M. Anpo, *J. Synchrotron Radiat.*, 2001, **8**, 608–609.
165 K. Ebitani, Y. Hirano and A. Morikawa, *J. Catal.*, 1995, **157**, 262–265.
166 L. Obalová, M. Šihor, P. Praus, M. Reli and K. Kočí, *Catal. Today*, 2014, **230**, 61–66.
167 M. Valášková, K. Kočí and J. Kupková, *Microporous Mesoporous Mater.*, 2015, **207**, 120–125.
168 K. Kočí, M. Reli, I. Troppová, M. Šihor, J. Kupková, P. Kustrowski and P. Praus, *Appl. Surf. Sci.*, 2017, **396**, 1685–1695.
169 M. Reli, L. Svoboda, M. Šihor, I. Troppová, J. Pavlovský, P. Praus and K. Kočí, *Environ. Sci. Pollut. Res. Int.*, 2018, **25**, 34839–34850.
170 K. Kočí, M. Reli, I. Troppová, M. Šihor, T. Bajcarová, M. Ritz, J. Pavlovský and P. Praus, *Catalysts*, 2019, **9**, 735.
171 V. Matějka, M. Šihor, M. Reli, A. Martaus, K. Kočí, M. Kormunda and P. Praus, *Mater. Sci. Semicond. Process.*, 2019, **100**, 113–122.
172 P. Praus, J. Lang, A. Martaus, L. Svoboda, V. Matějka, M. Kormunda, M. Šihor, M. Reli and K. Kočí, *J. Inorg. Organomet. Polym.*, 2019, **29**, 1219–1234.
173 L. Wang, W. Song, J. Deng, H. Zheng, J. Liu, Z. Zhao, M. Gao and Y. Wei, *Nanoscale*, 2018, **10**, 6024–6038.
174 W. Song, L. Wang, Y. Gao, J. Deng, M. Jing, H. Zheng, J. Liu, Z. Zhao, M. Gao and Y. Wei, *J. Mater. Chem. A*, 2018, **6**, 19241–19255.
175 L. Wang, J. Liu, W. Song, H. Wang, Y. Li, J. Liu, Z. Zhao, J. Tan, Z. Duan and J. Deng, *Chem. Eng. J.*, 2019, **366**, 504–513.
176 J. Liu, L. Wang, W. Song, M. Zhao, J. Liu, H. Wang, Z. Zhao, C. Xu and Z. Duan, *ACS Sustainable Chem. Eng.*, 2019, **7**, 2811–2820.
177 D. F. Swearer, H. Robatjazi, J. M. P. Martirez, M. Zhang, L. Zhou, E. A. Carter, P. Nordlander and N. J. Halas, *ACS Nano*, 2019, **13**, 8076–8086.
178 A. Klerke, C. H. Christensen, J. K. Nørskov and T. Vegge, *J. Mater. Chem.*, 2008, **18**, 2304–2310.
179 Q. Wang, J. Guo and P. Chen, *J. Energy Chem.*, 2019, **36**, 25–36.
180 F. Schüth, R. Palkovits, R. Schlögl and D. S. Su, *Energy Environ. Sci.*, 2012, **5**, 6278–6289.
181 X. Cui, C. Tang and Q. Zhang, *Adv. Energy Mater.*, 2018, **8**, 1800369.
182 Q. Han, H. Jiao, L. Xiong and J. Tang, *Adv. Mater.*, 2021, **2**, 564–581.
183 E. Stokstad, *Science*, 2014, **343**, 238.
184 K. Vikrant, K.-H. Kim, F. Dong and D. A. Giannakoudakis, *ACS Catal.*, 2020, **10**, 8683–8716.
185 S. Zhang, Z. He, X. Li, J. Zhang, Q. Zang and S. Wang, *Nanoscale Adv.*, 2020, **2**, 3610–3623.
186 H. Yuzawa, T. Mori, H. Itoh and H. Yoshida, *J. Phys. Chem. C*, 2012, **116**, 4126–4136.
187 A. Utsunomiya, A. Okemoto, Y. Nishino, K. Kitagawa, H. Kobayashi, K. Taniya, Y. Ichihashi and S. Nishiyama, *Appl. Catal., B*, 2017, **206**, 378–383.
188 A. C. Sola, D. Garzón Sousa, J. Araña, O. González Díaz, J. M. Doña Rodríguez, P. Ramírez de la Piscina and N. Homs, *Catal. Today*, 2016, **266**, 53–61.
189 H. Mozzanega, J. M. Herrmann and P. Pichat, *J. Phys. Chem.*, 1979, **83**, 2251–2255.
190 M. A. Kebede, N. K. Scharko, L. E. Appelt and J. D. Raff, *J. Phys. Chem. Lett.*, 2013, **4**, 2618–2623.
191 B. Boulinguiez, A. Bouzaza, S. Merabet and D. Wolbert, *J. Photochem. Photobiol., A*, 2008, **200**, 254–261.
192 M. Chen, J. Ma, B. Zhang, F. Wang, Y. Li, C. Zhang and H. He, *Appl. Catal., B*, 2018, **223**, 209–215.
193 G. Zhang, J. Ruan and T. Du, *ACS ES&T Eng.*, 2021, **1**, 310–325.
194 J. Feng, X. Zhang, G. Zhang, J. Li, W. Song and Z. Xu, *Chemosphere*, 2021, **274**, 129689.
195 X. Zhu, S. R. Castleberry, M. A. Nanny and E. C. Butler, *Environ. Sci. Technol.*, 2005, **39**, 3784–3791.
196 R. Zellner and I. W. M. Smith, *Chem. Phys. Lett.*, 1974, **26**, 72–74.
197 E.-M. Bonsen, S. Schroeter, H. Jacobs and J. C. Broekaert, *Chemosphere*, 1997, **35**, 1431–1445.
198 S. Kim and W. Choi, *Environ. Sci. Technol.*, 2002, **36**, 2019–2025.
199 J. Lee, H. Park and W. Choi, *Environ. Sci. Technol.*, 2002, **36**, 5462–5468.

200 H.-H. Ou, M. R. Hoffmann, C.-H. Liao, J.-H. Hong and S.-L. Lo, *Appl. Catal., B*, 2010, **99**, 74–80.

201 H. Kominami, H. Nishimune, Y. Ohta, Y. Arakawa and T. Inaba, *Appl. Catal., B*, 2012, **111–112**, 297–302.

202 A. C. A. de Vooys, M. T. M. Koper, R. A. van Santen and J. A. R. van Veen, *J. Electroanal. Chem.*, 2001, **506**, 127–137.

203 J. Nemoto, N. Gokan, H. Ueno and M. Kaneko, *J. Photochem. Photobiol., A*, 2007, **185**, 295–300.

204 Y. Shiraishi, S. Toi, S. Ichikawa and T. Hirai, *ACS Appl. Nano Mater.*, 2020, **3**, 1612–1620.

205 L. Qing-shui, D. Kazunari, N. Shuichi, O. Takaharu and T. Kenzi, *Chem. Lett.*, 1983, **12**, 321–324.

206 M. Reli, M. Edelmannová, M. Šihor, P. Praus, L. Svoboda, K. K. Mamulová, H. Otoupalíková, L. Čapek, A. Hospodková, L. Obalová and K. Kočí, *Int. J. Hydrogen Energy*, 2015, **40**, 8530–8538.

207 A. Iwase, K. Ii and A. Kudo, *Chem. Commun.*, 2018, **54**, 6117–6119.

208 M. Kaneko, N. Katakura, C. Harada, Y. Takei and M. Hoshino, *Chem. Commun.*, 2005, 3436–3438.

209 J. Zheng, T. Lu, T. M. Cotton and G. Chumanov, *J. Phys. Chem. B*, 1999, **103**, 6567–6572.

210 Y. Kim, E. B. Creel, E. R. Corson, B. D. McCloskey, J. J. Urban and R. Kostecki, *Adv. Energy Mater.*, 2018, **8**, 1800363.

211 H. Wang and J. A. Turner, *Energy Environ. Sci.*, 2013, **6**, 1802–1805.

212 M. Kan, D. Yue, J. Jia and Y. Zhao, *Electrochim. Acta*, 2015, **177**, 366–369.

213 E. Kecsenovity, S. T. Kochuveedu, J.-P. Chou, D. Lukács, Á. Gali and C. Janáky, *Sol. RRL*, 2021, **5**, 2000418.

214 R. Saito, H. Ueno, J. Nemoto, Y. Fujii, A. Izuoka and M. Kaneko, *Chem. Commun.*, 2009, 3231–3233.

215 H.-Y. Cheng, X.-D. Tian, C.-H. Li, S.-S. Wang, S.-G. Su, H.-C. Wang, B. Zhang, H. M. A. Sharif and A.-J. Wang, *Environ. Sci. Technol.*, 2017, **51**, 12948–12955.

216 S. Su, Y. Zhang, W. Hu, X. Zhang, D. Ju, C. Jia and J. Liu, *Bioelectrochemistry*, 2020, **132**, 107439.

217 M. Kaneko, N. Gokan, N. Katakura, Y. Takei and M. Hoshino, *Chem. Commun.*, 2005, 1625–1627.

218 X. Fan, Y. Zhou, G. Zhang, T. Liu and W. Dong, *Appl. Catal., B*, 2019, **244**, 396–406.

219 C. Yan and L. Liu, *J. Hazard. Mater.*, 2020, **388**, 121793.

220 Y. Qu, X. Song, X. Chen, X. Fan and G. Zhang, *Chem. Eng. J.*, 2020, **382**, 123048.